Structural Health Monitoring
XX(X):1–19

DOI: 10.1177/ToBeAssigned
www.sagepub.com/
SAGE

Synergistic application of operational modal analysis and ambient noise deconvolution interferometry for structural and damage identification in historic masonry structures: three case studies of Italian architectural heritage

Enrique García-Macías[1],Alban Kita[1] and Filippo Ubertini[1]

Abstract

Conservation techniques within the framework of Structural Health Monitoring (SHM), particularly through dynamic measurements and Operational Modal Analysis (OMA), are becoming popular for condition-based maintenance and decision making in historic structures. Nonetheless, while effective for giving insight into the overall behaviour of structures, these techniques may fail at detecting local damages with limited effects on the modal features of the system. In this regard, the analysis of propagating waves throughout the structure poses an attractive alternative for data-driven damage identification. Specifically, some encouraging results have been reported on the application of Seismic Interferometry to reinforced-concrete structures, albeit the number of works concerning ambient vibrations is far scarce, and practically nonexistent in the realm of historic structures. In this light, this paper explores the synergistic application of OMA and Ambient Noise Deconvolution Interferometry for the structural identification of historic structures through three different case studies, namely the Sciri Tower in Perugia, the Consoli Palace in Gubbio, and the bell-tower of the Basilica of San Pietro in Perugia. The first case study represents a typical example of a masonry tower inserted into a building aggregate, while the second one constitutes a particular case of a monumental masonry palace. The presented results and discussion cover diverse aspects of the identification of wave velocities, signal processing strategies, effects of dispersion, and robustness of the identification. Finally, the case study of the bell-tower of the Basilica of San Pietro illustrates the application of OMA and deconvolution interferometry for damage identification. To do so, two different ambient vibration tests conducted before and after the 2016 Central Italy seismic sequence are studied. The results show concentrated reductions in the wave velocities in the area of the belfry, which demonstrates that deconvolution interferometry constitutes a complementary technique to OMA for damage localization and, to some extent, damage quantification.

Keywords

Ambient vibration testing, Damage identification, Seismic Interferometry, Structural Health Monitoring, Wave propagation

1 Introduction

Historic structures constitute a fundamental asset of the cultural heritage and represent a valuable resource of social identity, shared spaces of remembrance, integration, and cohesion, as well as important economic activities derived from their fruition. Their preservation and safeguarding must ensure the structural safety needs, while respecting their historical and cultural values. In this context, SHM techniques have proved to provide an efficient solution to interrogate the integrity of structures, comprising Non-Destructive Testing (NDT) and damage identification tools suitable for decision making and condition-based maintenance [1–3]. In the realm of masonry heritage structures, SHM strategies based on Output-only or Operational Modal Analysis (OMA) have received most attention. These techniques exploit ambient acceleration records to extract the modal features of the system, namely the natural frequencies, mode shapes, and damping ratios [4,5]. The impact of these techniques on the monitored structures is kept minimal, and plenty of successful applications to diverse historic structures can be found in the literature, including bridges [6,7], towers [8,9], churches [10], and buildings [11,12]. Given that the modal features depend upon the stiffness, mass distribution and boundary conditions of the structure, damage detection through OMA can be performed by tracking variations in the identified modal parameters [13,14]. While highly effective in the identification of damage affecting the global stiffness

[1]Department of Civil and Environmental Engineering, University of Perugia, Italy

Corresponding author:
Enrique García-Macías, Department of Civil and Environmental Engineering, University of Perugia, Via G Duranti 93, Perugia 06125, Italy.
Email: enrique.garciamacias@unipg.it

of structures, OMA may fail at detecting local defects with limited effect on the modal features of the system.

Recent studies report Seismic Interferometry to be a promising technique for damage identification of structures. Originally proposed in Geophysics[15] to analyse the propagation of elastic waves in the earth's subsurface, this technique conceives the response of a dynamic system as a superposition of propagating waves, reflecting from its boundaries and interfering[16,17]. This technique is aimed in essence at constructing the Green's functions describing the propagation of waves between a set of receivers (e.g. geophones, hydrophones, or accelerometers) deployed throughout the monitored structure[18]. Since the scattering and attenuation of the waveforms depend upon the constitutive properties of the medium, the identification of wave velocities provides an indirect evaluation of the intrinsic stiffness of the system and, thus, structural damage can be related to local wave delays between pairs of sensors. The determination of waveforms can be conducted using cross-correlation, cross-coherence or deconvolution techniques[19]. In particular, deconvolution interferometry has been reported to be well-suited for the monitoring of mono-dimensional structures such as buildings[20–22]. It is important to note that this technique differs from ultrasonic testing (UT) techniques, which exploit the pulse/echo properties of high-frequency sound waves. In this case, the use of generators is imperative and waves are quickly attenuated, whereby UT limits to the characterization of small specimens[23]. Conversely, given that seismic waves exhibit larger wavelengths ($\approx 5 - 500$ m) and experience little attenuation, Seismic Interferometry can be used to characterize a full-scale building without any need for external actuators[24].

While still in the early stages, the application of seismic interferometric techniques to the monitoring of buildings has been reported to offer promising advantages compared to OMA-based approaches. Firstly, unlike modal methods, wave propagation approaches are insensitive to soil-structure interaction effects[25–28]. Therefore, the structural assessment is restricted to the integrity of the structure irrespective of the boundary conditions at the foundation. Moreover, damage-induced stiffness losses lead to local delays in the waveform propagating through the damaged part of the structure, whereby damage identification using Seismic Interferometry is local in essence[20–22,29]. Most interestingly, damage identification (detection, localization and, to some extent, quantification) can be performed in a fully data-driven way by peak-picking analysis of wave arrival times at different sensors' positions. Therefore, depending on the desired resolution of the damage identification (minimum two sensors), it is possible to devise sensing networks capable of tracking wave delays between pairs of sensors and, in this way, identify damages without the need of any simulation model. Conversely, modal methods are chiefly effective for estimating global damage, while the identification of local defects usually requires the inverse calibration of numerical models or metamodels (see e.g.[30,31]).

Most publications in the literature on the application of wave propagation methods to structural identification focus on reinforced concrete (RC) buildings under earthquake actions. It is worth noting the work by Trifunac *et al.*[32] who investigated the propagating waves in a 7-storey RC building located in California, US, during the Northridge M_w 6.4 earthquake in 1994. Their results demonstrated that earthquake-induced damage can be identified in the shape of local decreases in wave velocities between pairs of sensors. Kohler *et al.*[33] applied deconvolution interferometry for the system identification of a 17-storey moment-resisting steel-frame building located at the University of California. Through a dense sensor network of 72 accelerometers, those authors obtained the deconvolved waveforms of the building, usually termed impulse response functions (IRFs), for 20 different seismic inputs of small and moderate intensities. Another noteworthy contribution was done by Todorovska and Trifunac[20] who investigated the effects of earthquake-induced damage on the wave travel times of a 6-storey RC building in El Centro (California, US). Their results reported good correlation between the wave delays obtained by peak-picking analysis and the observed earthquake-induced damage. Snieder and Şafak[25] developed an equivalent uniform shear beam model to interpret the propagating waveforms in the 9-storey RC Millikan Library in Pasadena (Los Angeles, US) under the Yorba Linda M_w 4.3 earthquake in 2002. Similarly, Ebrahimian and Todorovska[34,35] developed a layered Timoshenko beam model for the system identification of multi-storey buildings based on seismic wave propagation analysis. Good agreement with experimental data was reported for a 54-storey steel-frame building[35] and the Millikan Library[36], and their results demonstrated the contribution of bending deformation to the dispersion of travelling waves (i.e. the variation of wave velocities with frequency).

The application of deconvolution interferometry to ambient vibration monitoring of structures is a still-developing area of research, and the number of experiences reported in the literature is very limited. In this regard, it is worth noting the work by Prieto *et al.*[37] who investigated the propagating ambient noise waves in a 17-storey steel moment-frame building located at the University of California. To that purpose, those authors proposed an ambient noise interferometric technique based on temporal averaging of deconvolved ambient vibration records divided into overlapping windows. Similarly, Nakata and Snieder[38] applied ambient noise deconvolution interferometry to an 8-storey building in Japan. Their results demonstrated that, unlike the case of seismic inputs, the presence of several internal excitation sources (e.g. wind actions or human activities) leads to waveforms that exhibit causal and acausal pulses for virtual sources both at the base and the roof levels. Bindi *et al.*[39] applied non-parametric identification methods, including ambient deconvolution interferometry and frequency domain decomposition, to assess the dynamic behaviour of an 8-storey RC hospital in northern Greece. Sun and co-authors[40] proposed a Bayesian model updating approach based upon deconvolved IRFs from ambient vibrations, and its effectiveness was demonstrated with a case study of a 21-storey RC building. More recently, Lacanna *et al.*[41] reported the application of OMA and seismic interferometry for the system identification of Giotto's bell-tower in Florence (Italy). Their results demonstrated the superior capability of the coupled application of these

techniques to perform a complete assessment of the dynamic response of structures.

In light of the afore-presented literature review, it is concluded that, while considerable effort has been devoted to the monitoring of RC buildings through deconvolution interferometry, the number of applications to masonry structures is far scarce. Furthermore, as reported in the pioneering work of Lacanna *et al.*[41], effective data processing techniques and the effects of dispersion on masonry structures still have to be studied in depth. In order to address this issue, most aspects covering the identification of ambient noise waves in masonry structures are investigated in this paper through three case studies of Italian historic structures, including the Sciri Tower located in Perugia, the Consoli Palace located in Gubbio and, finally, the bell-tower of the Basilica of San Pietro also located in Perugia. The first case study constitutes an illustrative example of a standard masonry tower inserted into a building aggregate. An ambient vibration test (AVT) is used for OMA and deconvolution interferometry accounting for the influence of signal filtering, dispersion, as well as the robustness of the identification for increasing data acquisition sampling rates. Afterwards, the Consoli Palace is presented as a case study of a complex masonry building with limited distance between sensors. In this case, the studies focus on the robustness of the identification of wave velocities through peak-picking analysis for increasing monitoring times and sampling frequencies. Finally, the bell-tower of the Basilica of San Pietro is presented as a case study of coupled application of OMA and ambient noise interferometry for damage identification. According to the research work of Ubertini and co-authors[14], the 2016 Central Italy seismic sequence caused a slight structural damage manifesting as resonant frequency decays that are identifiable by long-term OMA techniques. In this paper, two different AVTs conducted in February 2015 and May 2017, that is before and after the seismic sequence, are used for performing OMA and ambient noise deconvolution interferometry. The results demonstrate that, while OMA only allows for damage detection, deconvolution interferometry constitutes a complementary technique for damage localization and, to some extent, damage quantification.

The remaining of this paper is organised as follows. Section 2 overviews the fundamentals of ambient noise deconvolution interferometry. Sections 3, 4 and 5 present the analysis results of the case studies of the Sciri Tower, the Consoli Palace and the bell-tower of the Basilica of San Pietro, respectively. Finally, Section 6 concludes this work.

2 Deconvolution interferometry using ambient vibration

2.1 Transfer functions and impulse response functions

Let us consider a masonry structure equipped with an array of sensors monitoring its response $u(z,t)$ along the height $0 \leq z \leq H$, where t is the time variable and H the total height of the structure as sketched in Fig. 1. Deconvolution interferometry allows getting insight into the propagation of shear waves between two arbitrary sensors, considering one sensor at level z_{ref} as reference input signal $u(z_{ref},t)$ and the other at level z as output signal $u(z,t)$. Assuming that the structure behaves as a linear time-invariant system, the reference and output signals can be related in the time domain t as[20]:

$$u(z,t) = u(z_{ref},t) * h(z,z_{ref},t) = \int_0^t u(z_{ref},s)\, h(z,z_{ref},t-s)\,\mathrm{d}s, \tag{1}$$

or, alternatively, in the frequency domain ω as:

$$\widehat{u}(z,\omega) = \widehat{u}(z_{ref},\omega)\,\widehat{h}(z,z_{ref},\omega), \tag{2}$$

where $*$ indicates convolution, and a hat indicates Fourier transform. Functions $\widehat{h}(z,z_{ref},\omega)$ and $h(z,z_{ref},t)$ denote the transfer function (TF) and the impulse response function (IRF) between the output signal $u(z,t)$ and the input signal $u(z_{ref},t)$, respectively. The IRFs physically relate the responses of the system at different levels z to a virtual Dirac Delta impulse $\delta(t)$ at level z_{ref}. In other words, these functions represent the Green's functions of the system and characterize the propagation of an input pulse applied at z_{ref} among the receivers deployed in the structure[19]. The IRFs can be computed by taking the inverse Fourier transform of the corresponding TFs as follows:

$$h(z,z_{ref},t) = \mathscr{F}^{-1}\left\{\widehat{h}(z,z_{ref},\omega)\right\} = \mathscr{F}^{-1}\left\{\frac{\widehat{u}(z,\omega)}{\widehat{u}(z_{ref},\omega)}\right\}, \tag{3}$$

with $\mathscr{F}^{-1}$ denoting the inverse Fourier transform operator. Nonetheless, the IRFs can be only obtained in practice for a finite frequency band $|\omega| < \omega_{max} = (Fs/2)2\,\pi$, with Fs being the sampling frequency, that is:

$$h(z,z_{ref},t) = \frac{1}{2\pi}\int_{-\omega_{max}}^{+\omega_{max}} \hat{h}(z,z_{ref},\omega)e^{-\mathrm{i}\omega t}\,\mathrm{d}\omega. \tag{4}$$

In addition, a regularized version of the TFs in Eq. (3) is usually introduced to avoid numerical instability due to division by null numbers as:

$$h(z,z_{ref},t) \approx \mathscr{F}^{-1}\left\{\frac{\widehat{u}(z,\omega)\,\overline{\widehat{u}(z_{ref},\omega)}}{\left|\widehat{u}(z_{ref},\omega)\right|^2+\epsilon}\right\}, \tag{5}$$

where the bar indicates complex conjugate, and ϵ denotes a regularization parameter. In this work, we use $\epsilon = 0.1\overline{P}$, with $\overline{P}$ being the average power spectrum of the reference input signal.

The velocity of the shear waves propagating in the structure can be computed by simple peak-picking analysis of the IRFs as illustrated in Fig. 1. To do so, the time-lag τ_i between the motion at level z_{i+1} and level z_i is obtained by peak-picking the maximum values of the IRFs $h(z_{i+1},z_{ref},t)$ and $h(z_i,z_{ref},t)$ along an identified ray path[24]. It can be proved that the time difference between the local maxima of $h(z_{i+1},z_{ref},t)$ and $h(z_i,z_{ref},t)$ maximizes the cross-correlation between $u(z_{i+1},t)$ and $u(z_i,t)$[36]. Then, the velocity of the pulses travelling between the sensors can be computed as $v_i = l_i/\tau_i$, with $l_i = z_i - z_{i+1}$. Finally, it is important to note that the response at any arbitrary level

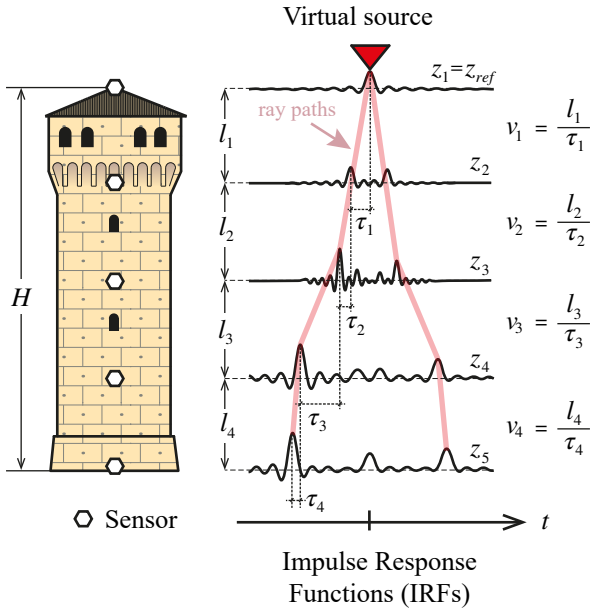

Figure 1. Schematic of the peak-picking analysis of a waveform obtained by deconvolution interferometry considering a virtual source at the roof level.

can be used as reference, usually termed a virtual source. Virtual sources are typically defined either at the base or the roof levels, and do not necessarily need to coincide with the physical source (e.g. the base accelerations induced by earthquakes). Furthermore, although acceleration records are often used to describe the propagation of seismic waves, other physical measurements can be also used such as displacements, velocities or strains.

2.2 Low-pass and band-pass filtering of IRFs

It has been reported in the literature that high-rise buildings may exhibit a dispersive behaviour[34]. This means that the wavenumber k and velocity of the propagating waves are functions of the frequency ω according to a certain dispersion relation. More specifically, the travelling waveform can be defined by the phase and group velocities as $c^p = \omega/k$ and $c^g = \partial\omega/\partial k$, respectively. The phase velocity determines the velocity of propagation of the pulses, while the group velocity defines the velocity of propagation of the envelopes of the waveforms. When the system is not dispersive, the phase and group velocities coincide, i.e. $c^p = c^g$. In order to identify the wave velocities in a dispersive structure, it is usually convenient to isolate the contribution of certain frequency bands to the computed waveforms. To do so, a band-pass filter $\widehat{S}$ can be applied to the TFs in the frequency domain as:

$$h(z, z_{ref}, t) = \mathscr{F}^{-1}\left\{\widehat{h}(z, z_{ref}, \omega)\,\widehat{S}(\omega, \omega_1, \omega_2)\right\}, \qquad (6)$$

with $\omega_2 > \omega_1$ denoting the cut-off frequencies. This filter can be defined as a shifted box function as follows:

$$\widehat{S}(\omega, \omega_1, \omega_2) = \begin{cases} 1 & \omega_1 \le |\omega| \le \omega_2 \\ 0 & \text{otherwise} \end{cases} \qquad (7)$$

Note that the incorporation of $S(\omega)$ into Eq. (2) implies that, at the reference level z_{ref}, the TF corresponds to the band-pass filter, that is $\widehat{h}(z_{ref}, z_{ref}, \omega) = \widehat{S}(\omega)$ or, alternatively, the IRF $h(z_{ref}, z_{ref}, t) = S(t)$. Figure 2 shows $S(t)$ and $\widehat{S}(f)$ for both low-pass and band-pass filtering, where $f = \omega/2\pi$. It is noted that the low-pass filter $S(t)$ in the time domain corresponds to a sinc function, with half-width of the central lobe $\Delta t = 1/2f_2$. On the other hand, the band-pass filter $S(t)$ in the time domain is a harmonic function modulated by a sinc function. The half-widths of the central lobe of $S(t)$ and its envelope are $\Delta t = 1/2f_s$ and $\Delta t_e = 1/2f_r$, respectively, with $f_s = (f_2 + f_1)/2$ and $f_r = (f_2 - f_1)/2$ the semi-sum and semi-difference of the cut-off frequencies. For clarity purposes, Figure 3 summarizes the calculation process of IRFs.

The clear identification of propagating pulses within a waveform is a key aspect in the assessment of wave velocities through a peak-picking approach. To do so, some practical considerations must be taken into account, including:

- *Assessment of phase and group velocities*: The identification of group velocities is more robust than the identification of phase velocities due to the higher smoothness of the envelopes of the IRFs. Nevertheless, given that masonry structures are characterized by large stiffness and, as a result, large wave velocities and short propagation times, and considering that in dispersive structures $c^g > c^p$ (see e.g.[34]), the identification of group velocities is often impractical. Therefore, the use of inverse calibration of wave propagation models usually becomes imperative for the identification of group velocities.

- *Minimum separation between sensors*: Two different propagating pulses can only be distinguished if there exists a sufficient time shift between their arrival times. In order to address this issue, let us focus on the case of an upward pulse reflecting off a free surface and propagating downward as illustrated in the bottom part of Fig. 2. If the structure is dispersive, the travel time of the pulses τ_p will give the phase velocity c^p, while the travel time of the envelopes τ_g will give the group velocity c^g. For generality, let us consider a band-pass filter with cut-off frequencies f_1 and f_2 as shown in Fig. 2 (b). If there is one single propagating mode in the frequency band (f_1-f_2), and if we consider that the half-width of the central lobe of the pulse quantifies the uncertainty of its time localization, two pulses can be only distinguished as separate processes if shifted in time more than the width of the central lobe. Therefore, the minimum separations between sensors to resolve the incident and reflected pulses l^p_{min} and propagating envelopes l^g_{min} read:

$$l^p_{min} = c^p/8f_s, \quad l^g_{min} = c^g/4f_r, \qquad (8)$$

whereby c^p and c^g can only be measured if f_s and f_r are large enough, respectively.

- *Maximum frequency of analysis*: Ebrahimian and Todorovska[34] demonstrated through an equivalent Timoshenko beam model for wave propagation

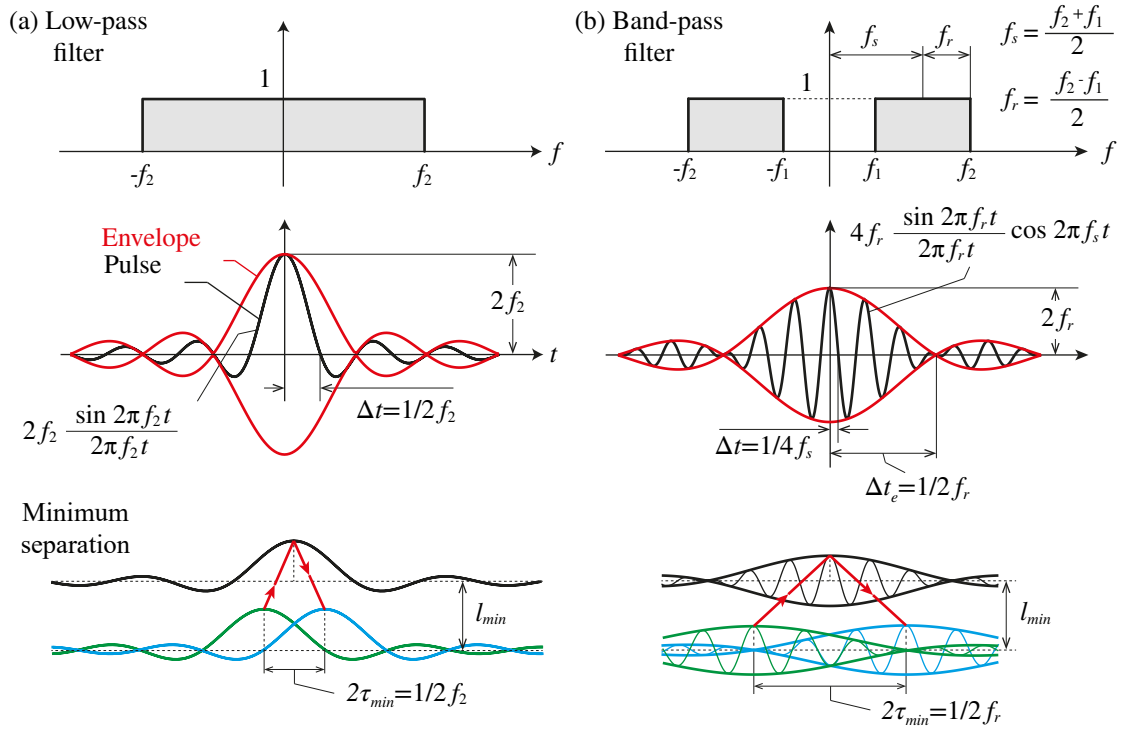

Figure 2. Virtual source function in the frequency ($f = \omega/2\pi$) and time (t) domains, for a box function (low-pass filter) (a) and shifted box function (band-pass filter) (b).

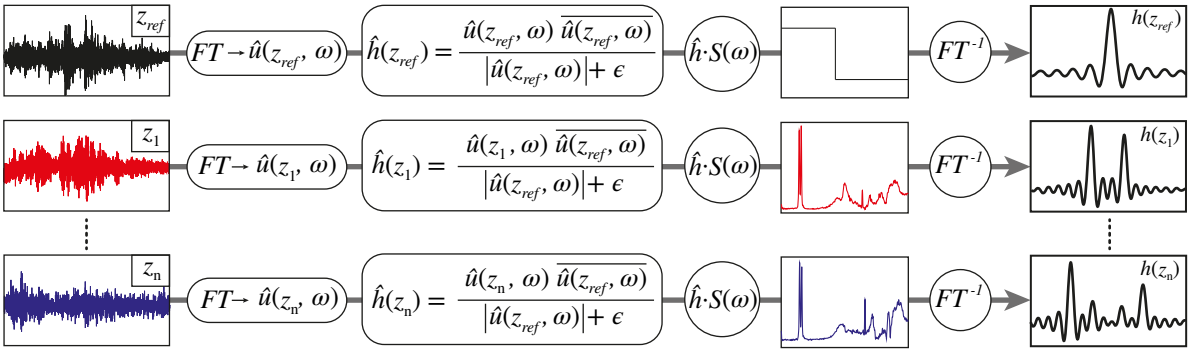

Figure 3. Flowchart of the calculation of IRFs through ambient noise deconvolution interferometry.

analysis in high-rise buildings the existence of a critical frequency $f_{cr} = c_s\sqrt{k_G}/r_g 2\pi$ (with c_s being the shear wave velocity in the material, k_G the shear correction factor of a Timoshenko beam equivalent to the building, and r_g the radius of gyration of the building). Above this critical frequency, a secondary wave propagation mode intervenes in the waveforms generating complex interference patters. In this paper, all the considered frequency bands are below this critical frequency and no secondary modes have been observed (e.g. $f_{cr} \approx 46$ Hz for a building with similar geometrical and material properties to those of the Sciri Tower).

- *Minimum sampling frequency*: Considering a separation l between sensors, a travelling pulse can be only identified if the sampling frequency rate F_s satisfies the following condition:

$$F_s \geq c^{p,g}/l. \tag{9}$$

- *Minimum observable variations in wave velocities*: The suitability of a monitoring system for detecting damage-induced wave delays is highly conditioned by the sampling frequency. In particular, for a given wave velocity c and separation l between sensors, i.e. a wave lag $\tau = l/c$, a rough estimate of the relationship between the minimum observable reductions in the wave velocity δc and the sampling frequency F_s reads:

$$\delta c = -\frac{l}{F_s\tau^2 + \tau}. \tag{10}$$

2.3 Stacking approach for multiple-window ambient-vibration data

The extension of the previous formulation to the continuous monitoring of structures is of pivotal importance for the identification (detection, localization and quantification) of early-stage damages. To this aim, deconvolution interferometry can be applied to ambient-vibration records considering time windows of duration T, typically with a certain overlapping to minimize the variance of the estimates on the velocity of the travelling waves. Specifically, the deconvolved waveforms can be stacked (averaged) over N intervals of duration T as follows:

$$h(z, z_{ref}, t) = \frac{1}{N}\sum_{n=1}^{N}\left[\mathscr{F}^{-1}\left\{\frac{\widehat{u}_n(z,\omega)}{\widehat{u}_n(z_{ref},\omega)}\right\}\right] \approx \approx \frac{1}{N}\sum_{n=1}^{N}\left[\mathscr{F}^{-1}\left\{\frac{\widehat{u}(z,\omega)\overline{\widehat{u}(z_{ref},\omega)}}{\left|\widehat{u}(z_{ref},\omega)\right|^2+\epsilon}\right\}\right]. \quad (11)$$

3 Case I: The Sciri Tower

The first case study consists of the 41 m high civic tower located in the historical centre of Perugia in Italy, named *Torre degli Sciri* (see Fig. 4 (a)). The Sciri Tower was erected in the late 13$^{\text{th}}$ century for defensive purposes and, nowadays, it is the only remaining medieval tower in a good state of preservation in the city. Since its construction, the tower was owned by the noble family of Oddi. Nonetheless, after violent conflicts between noble houses that caused the exile of the Oddi family in October 1488, the ownership of the tower was transferred to the Sciri family who gave it its current name. In 1680, the tower and the adjoining building were gifted to the Franciscan Third Order until 2011, when the complex became property of the Municipality of Perugia.

The Sciri Tower forms part of a building aggregate with approximate plan dimensions of 21.8×24.6 m (see Fig. 4 (c)). The tower has a hollow rectangular cross-section of 7.15×7.35 m, with three façades connected to the adjacent masonry buildings up to a height of 17 m, and a fourth one remaining exposed all along its height. Made of homogeneous and regular squared white limestone blocks, the structure of the tower can be ideally divided into two structural portions. The lower part has wall thicknesses of 1.68 m and 2.1 m and rises up to 8.4 m. In this part, there are some small openings and a stone masonry vaulted slab that stands above the rooms of an old chapel. On the other hand, the upper part has slender continuous walls (with thickness varying in height from 1.6 m to 1.4 m), with four 1.5 m wide masonry vaulted landing slabs at different heights supporting a metal staircase with wooden treads. A brick masonry ceiling vault completes the tower, and a 0.5 m thick parapet extends up to a total height of 41 m.

In order to identify the modal parameters and the travelling pulses of the Sciri Tower, an AVT was carried out on May 22$^{\text{nd}}$ 2017 following the preliminary field tests reported by Kita *et al.*[42]. Figure 4 (b) shows the monitoring layout, which consisted of 12 high sensitivity (10 V/g) uniaxial PCB 393B12 accelerometers installed at four different heights of the tower, namely $z = 40.5$ m, $z = 33.5$ m, $z = 24.0$ m and $z = 8.4$ m. The acceleration data were acquired using a multi-channel data acquisition system (DAQ) model NI CompactDAQ-9184 with NI 9234 data acquisition modules for accelerometers (24-bit resolution, 102 dB dynamic range and anti-aliasing filters) located at the level $z = 36.7$ m. The ambient vibrations induced by traffic and wind actions in operational conditions were recorded for 90 minutes at a sampling frequency of 1652 Hz. Note that an auxiliary coordinate system with axes x' and y' is indicated in Fig. 4 (b) to facilitate the description of the mode shapes in the subsequent sections.

Table 1. Experimentally identified natural frequencies and damping ratios of the Sciri Tower from AVT by SSI.

Mode no.	Mode type	f_i^{SSI} [Hz]	ζ^{SSI} [%]
1	$F_{x'1}$	1.716	0.832
2	$F_{y'1}$	1.911	0.792
3	$F_{x'2}$	5.544	3.739
4	$F_{y'2}$	6.040	1.429
5	$T_{z'1}$	8.432	1.660
6	$F_{x'3}$	9.940	1.063
7	$F_{y'3}$	10.900	2.946

3.1 Identification of modal properties

Figure 5 depicts the raw ambient vibration records of channels 2, 5, 8 and 11 (a), the transfer functions with respect to the base level ($\widehat{h}(z, z_{ref}, f)$ with $z_{ref} = 8.40$ m) (b), and the coherence functions (c) in the y-direction. In addition, Table 1 summarizes the natural frequencies and damping ratios obtained by means of Stochastic Subspace Identification (SSI). Seven modes are found in the frequency range between 0 and 12 Hz, and the identified mode shapes are presented in Fig. 6. Specifically, two flexural modes are found in the x'-direction, $F_{x'1}$ and $F_{x'2}$, two flexural modes in the y'-direction, $F_{y'1}$ and $F_{y'2}$, one torsional mode, T_{z1}, and two higher order flexural modes, $F_{x'3}$ and $F_{y'3}$. As can be noted in Fig. 5 (b), the resonant frequencies of the Sciri Tower can be identified by the peak-picking analysis of the ambient noise TFs, yielding relative differences with those obtained by SSI below 1% (only 0.06% for the first two natural frequencies). This fact suggests that soil-structure interaction effects are negligible and, therefore, the tower can be assumed as fixed at the base.

3.2 Low-pass filtered versus band-pass filtered IRFs

In the first place, low-pass filtered IRFs have been obtained with the 90 min long ambient acceleration records down-sampled to $F_s = 200$ Hz as shown in Fig. 7. In order to assess the degree of dispersion, different cut-off frequencies have been considered, namely 6 Hz, 10 Hz, 14 Hz, 18 Hz and 22 Hz. The broadest frequency range, 0-22 Hz, covers the full range of expected motions, whereas the narrowest band, 0-6 Hz, emphasizes the first bending modes of the Sciri Tower (see Table 1). The IRFs have been obtained in both x and y directions as shown in Figs. 7 (a) and (b), respectively, considering virtual sources at both the roof (VSR, $z_{ref} = 40.5$ m) and base levels (VSB, $z_{ref} = 8.4$ m). It is observed that the waveforms obtained for virtual sources at the roof level exhibit acausal upgoing waves (in negative times) and causal downgoing waves (in positive times). This behaviour

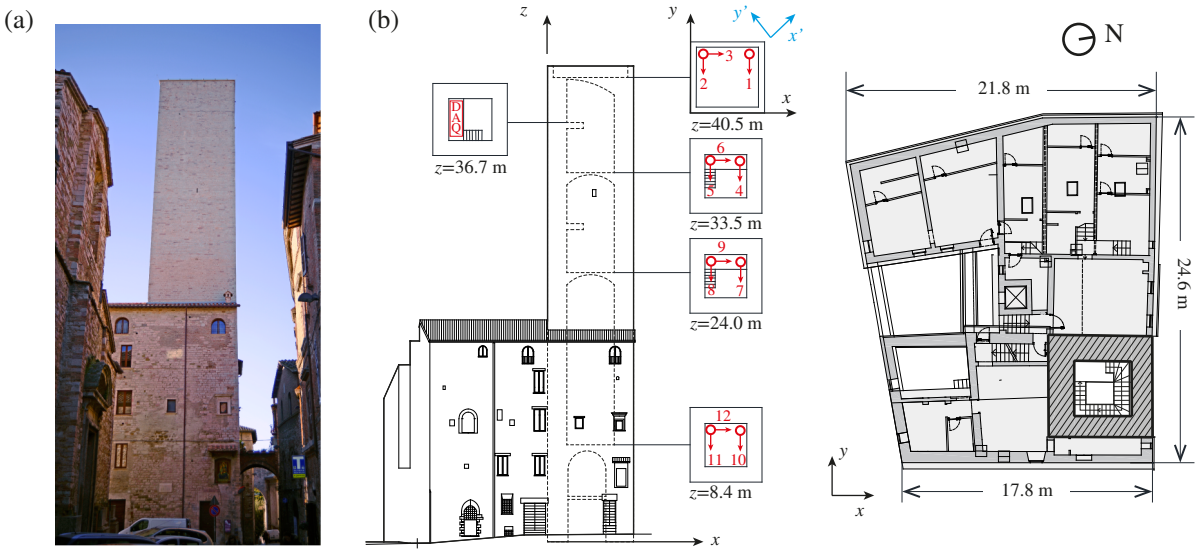

Figure 4. View of the Sciri Tower (a), and sketch of the structural monitoring system (b) with sensors positions (from 1 to 12).

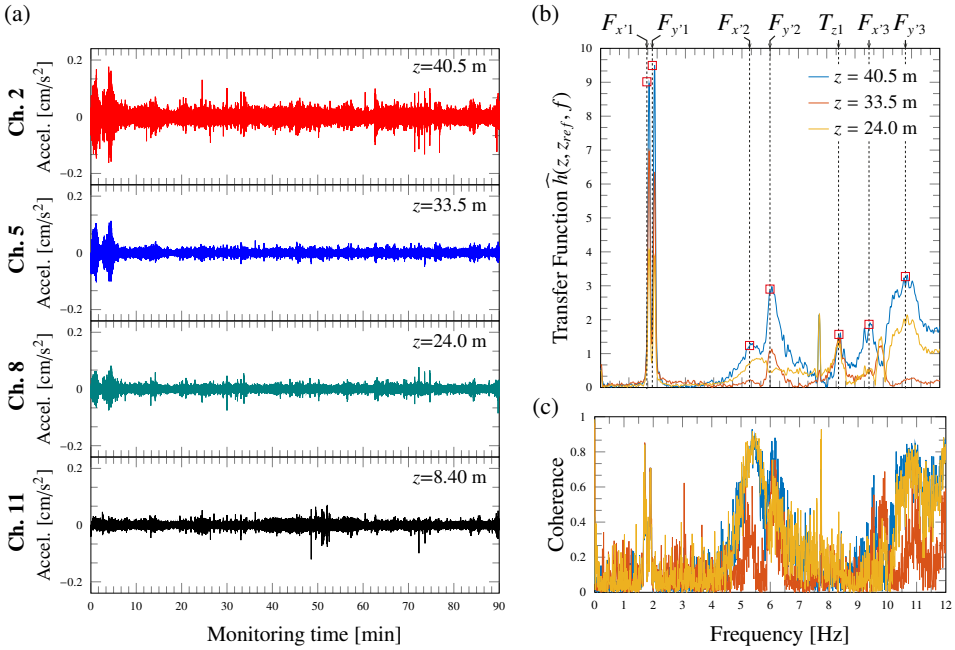

Figure 5. Ambient vibrations recorded by channels 2, 5, 8 and 11 (a), transfer functions with respect to the base level ($z = 8.40$ m) (b), and coherence functions (c) in the y-direction of the Sciri Tower.

coincides with the waveforms obtained from earthquake data as shown by Snieder and Safak[25]. Similarly, the waveforms obtained for virtual sources at the base level also show upward and downward travelling pulses. This behaviour differs from the waveforms obtained under seismic records, where only causal pulses propagate with multiple reflections at the base and roof levels[25]. Contrarily, ambient vibrations are characterized by multiple sources inside and outside the structure[38] (e.g. micro-tremors, wind loads, human actions, or other vibrations of entropic nature), which originates the presence of causal and acausal pulses when virtual sources are considered at the base level. It can be also visually noted in Fig. 7 that pulses travel faster for larger frequencies. This fact is indicative of a dispersive behaviour, which may be due to a relevant contribution of bending deformation[34], and/or to the interference of the aggregate building.

In general, waves propagate in three directions throughout the structure with multiple reflections from the boundaries and nonhomogeneities. Nevertheless, the relative simplicity of the waveforms previously presented in Fig. 7 suggests that the wave propagation is predominantly one-dimensional and, therefore, the wave velocities can be computed by simple peak-picking analysis. In this light, Table 2 reports the pulse travel times, τ_i, and wave velocities, v_i, computed by peak-picking analysis as the average of the downgoing and upgoing pulses. Overall, it is observed that the velocity of the waves crossing the whole tower increases with frequency, which confirms the previous discussion on the contribution of dispersion to the wave propagation. The propagating pulses within the tower cannot be resolved for the frequency bands 0-6 Hz and 0-10 Hz, where the considerable width of the source pulses precludes the identification of separate

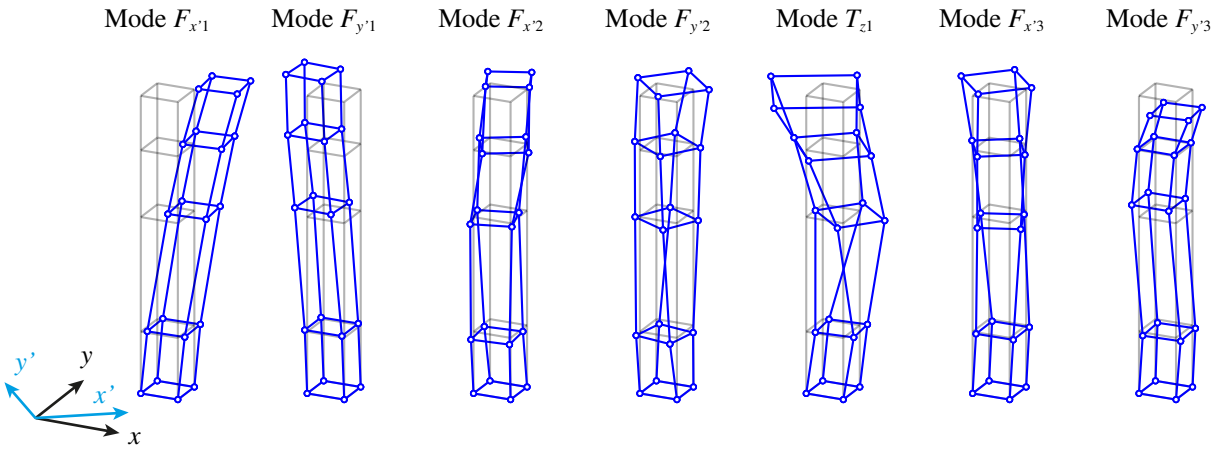

Figure 6. Experimentally identified vibration modes of the Sciri Tower.

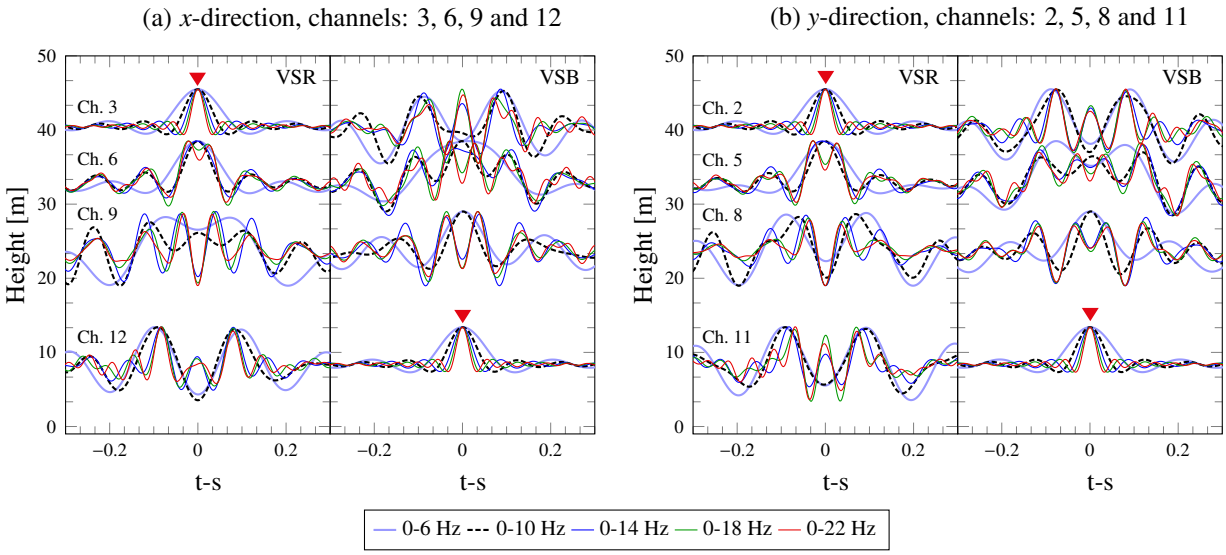

Figure 7. Low-pass filtered IRFs in the x- (a) and y- (b) directions of the Sciri Tower considering different frequency bands (F_s=200 Hz).

travelling pulses (see Fig. 7). It is also noted in Table 2 that, although the stiffness of the Sciri Tower is slightly larger in the x-direction, the wave velocities in the bottom layers L2 and L3 (8.4 m $< z <$ 33.5 m) are higher in the y-direction. Therefore, it is concluded that the restraint imposed by the building aggregate is stiffer in the y-direction, whereas the wave velocities are higher in the x-direction in the top layer L1 of the tower (33.5 m $< z <$ 40.5 m) where no contribution of the building aggregate exists. These results evidence one of the most notable features of deconvolution interferometry, relating the local nature of shear wave velocities and, as a result, the possibility of conducting system and damage identification without the support of any theoretical model. Finally, it is important to note that considerable discrepancies are found between the wave velocities along the tower, which may be due to sampling limitations because of the short separation between the receivers and the high velocity of the pulses.

The identification of wave velocities considering band-pass filtered IRFs is presented in Fig. 8. In particular, three different frequency bands are investigated, namely 1-7 Hz, 3-14 Hz and 9-14 Hz. It is important to note that, given the low frequencies of the first bending modes ($f_1^{\text{SSI}} = 1.715$ Hz and $f_2^{\text{SSI}} = 1.911$ Hz) and the limited distance between the sensors, travelling pulses in frequency bands isolating the modes $F_{x'1}$ and $F_{y'1}$ cannot be resolved. Thus, the first frequency band (1-7 Hz) includes the contribution of the first and second bending modes. The second frequency band (3-14 Hz) retains the torsional mode along with the second and third bending modes and, finally, the third band (9-14 Hz) only includes the higher order flexural modes. In addition, the envelopes of the IRFs computed by Hilbert transform are also included. Note that, according to the previous discussion in Section 2.2, the width of the envelopes increases with f_r, that is the width of the box filter. Thereby, the envelopes of the travelling pulses in Fig. 8 can be only identified in the second band 3-14 Hz with the maximum frequency width of 11 Hz. In this case, the group velocity in the $y-$direction can be computed as $c^g = 32.1/\tau^g = 458.57$ m/s, while the phase velocity takes the value $c^p = 32.1/\tau^p = 442.76$ m/s (see insert in Fig. 8 (b)). Typically, it results that $c^g > c^p$ as extensively reported in the literature (see

Table 2. Measured wave velocities, v_i, in the x- and y-directions of the Sciri Tower from pulse travel times, τ_i, in different frequency bands (F_s=200 Hz).

x-direction, channels: 3, 6, 9 and 12			0-6 Hz		0-10 Hz		0-14 Hz		0-18 Hz		0-22 Hz	
Layer	z_{i+1} - z_i [m]	l_i [m]	τ_i [ms]	v_i [m/s]	τ_i [ms]	v_i [m/s]	τ_i [ms]	v_i [m/s]	τ_i [ms]	v_i [m/s]	τ_i [ms]	v_i [m/s]
L1	33.5 - 40.5	7.0	-	-	-	-	-	-	12.50	875.00	15.00	622.22
L2	24.0 - 33.5	9.5	-	-	-	-	40.00	237.50	26.25	443.33	20.00	779.49
L3	8.4 - 24.0	15.6	-	-	-	-	37.50	423.53	40.00	396.19	45.00	356.57
Total			95.00	337.89	83.75	383.28	82.50	389.09	78.75	407.62	80.00	401.25
y-direction, channels: 2, 5, 8 and 11			0-6 Hz		0-10 Hz		0-14 Hz		0-18 Hz		0-22 Hz	
Layer	z_{i+1} - z_i [m]	l_i [m]	τ_i [ms]	v_i [m/s]	τ_i [ms]	v_i [m/s]	τ_i [ms]	v_i [m/s]	τ_i [ms]	v_i [m/s]	τ_i [ms]	v_i [m/s]
L1	33.5 - 40.5	7.0	-	-	-	-	13.75	550.00	18.75	477.27	20.00	407.27
L2	24.0 - 33.5	9.5	-	-	-	-	32.50	294.05	21.25	538.33	16.25	823.33
L3	8.4 - 24.0	15.6	-	-	-	-	38.75	403.00	32.50	482.86	35.00	445.71
Total			90.00	356.67	93.75	342.40	85.00	377.65	72.50	442.76	71.25	450.53

Table 3. Assessed global wave velocities in the x- and y-directions of the Sciri Tower considering different frequency bands (F_s=200 Hz).

	x-direction			y-direction		
	1-7 Hz	3-14 Hz	9-14 Hz	1-7 Hz	3-14 Hz	9-14 Hz
τ [ms]	81.25	78.75	80.00	83.75	72.50	65.00
v [m/s]	395.08	407.62	401.25	383.28	442.76	493.85

e.g.[34]). Therefore, given that masonry structures are usually low- or moderate-rise constructions, the direct assessment of group velocities is frequently impractical. The velocities of the waves crossing the whole tower (averaged between the upgoing and downgoing pulses) are presented in Table 3.

3.3 Dispersion analysis

The contribution of dispersion to the wave propagation in the Sciri Tower is further investigated in Fig. 9. Specifically, Figs. 9 (a) and (b) depict the wave velocity in the x- and y-directions, respectively, for cut-off frequencies between 5 Hz and 30 Hz. The velocities have been obtained through peak-picking analysis of low-pass filtered IRFs, and averaged between causal and acausal pulses. In both cases, it is observed that, according to previously published theoretical results in the literature (e.g.[34]), the wave velocities increase with frequency until a certain limit in which they tend to an asymptotic value. The wave propagation in the $x-$direction is considerably less dispersive, reaching an asymptotic wave velocity at moderately low frequencies. Conversely, wave velocities in the $y-$direction require large frequencies to reach a stable value. Note that the velocity values previously reported in Table 3 for band-pass filtered IRFs follow the trend of the dispersion curves. In particular, the wave velocities obtained for the frequency bands 3-14 Hz and 9-14 Hz are biased towards the higher values of velocity in the frequency band. This fact agrees with previously reported results in the literature, such as the work of Ebrahimian *et al.*[36] who ascribed this behaviour to the particular type of dispersion found in beam-like structures. It is also interesting to note in Fig. 9 (b) that, at low frequencies ($f < 10$ Hz), the wave velocities exhibit a non monotonic behaviour. This may be due to the contribution of the building aggregate, generating complex waveforms at low frequencies. Finally, some differences are found between the velocities computed for VSR and VSB schemes, which may be due to limitations in the peak-picking analysis derived from the dispersion effect.

3.4 Convergence study on the data acquisition sampling rate

The robustness of the peak-picking assessment of the wave velocities for increasing sampling rates is investigated in Fig. 10. To do so, the layers' wave velocities and the total velocity of waves crossing the whole tower are studied in Figs. 10 (a) and (b), respectively, considering low-pass filtered IRFs with a cut-off frequency of 18 Hz. Overall, it is noted that the uncertainty of the assessed wave velocities decreases with increasing sampling frequencies. Specifically, it is observed in Fig. 10 (b) that the velocity of waves crossing the whole tower stabilizes at low sampling rates, and the estimates assuming virtual sources at the roof level (VSR) and at the base level (VSB) are very similar. More significant uncertainties are noted between the layers' velocities in Fig. 10 (a). For instance, it is observed that the wave velocity of the third layer (L3, 8.4 m $< z <$ 24.0 m) exhibits a fast convergence, and the estimates considering VSR and VSB schemes are very similar. Conversely, the estimates of the first layer (L1, 33.5 m $< z <$ 40.5 m) and the second layer (L2, 33.5 m $< z <$40.5 m) show maximum variations for the cases of VSB and VSR schemes, respectively. These differences can be explained by the separation between the sensors, which is maximum in the first layer (l_1 = 15.6 m) and, as a result, the accuracy and robustness of the estimates are maximum in this layer. Conversely, layers L1 and L2 have shorter lengths of 7 m and 9.5 m, respectively, thereby the uncertainty in the determination of wave velocities in these layers is larger.

3.5 Modal analysis through deconvolution interferometry

As the final meaningful result obtained for the Sciri Tower, Fig. 11 illustrates the potential of ambient noise deconvolution interferometry to assess other modal features of the structure, such as the mode shapes or damping ratios. In particular, this analysis focuses on the y-direction of the tower, although similar conclusions can be achieved in the x-direction. Firstly, damping properties can be inferred from

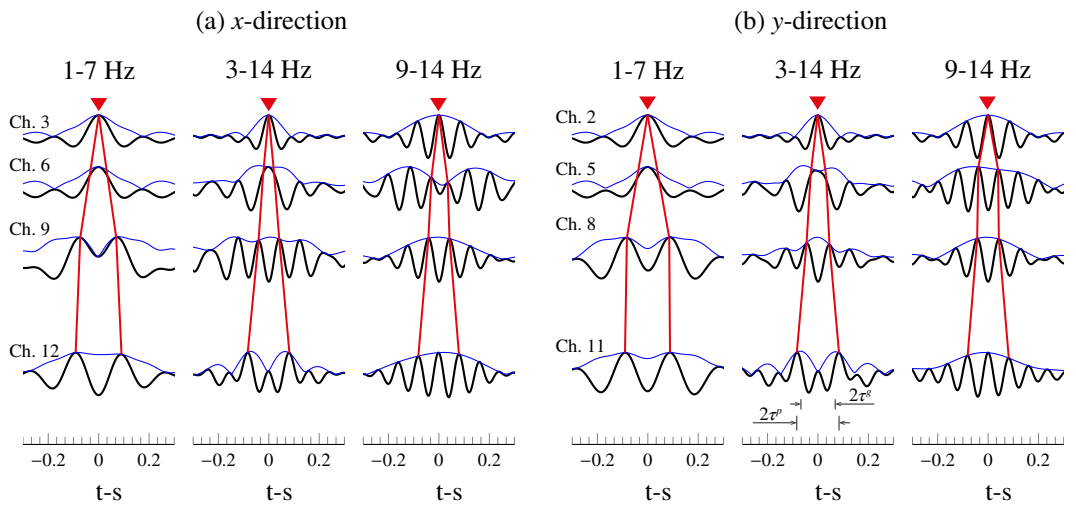

Figure 8. Band-pass filtered IRFs in the x- (a) and y- (b) directions of the Sciri Tower considering different frequency bands (F_s=200 Hz).

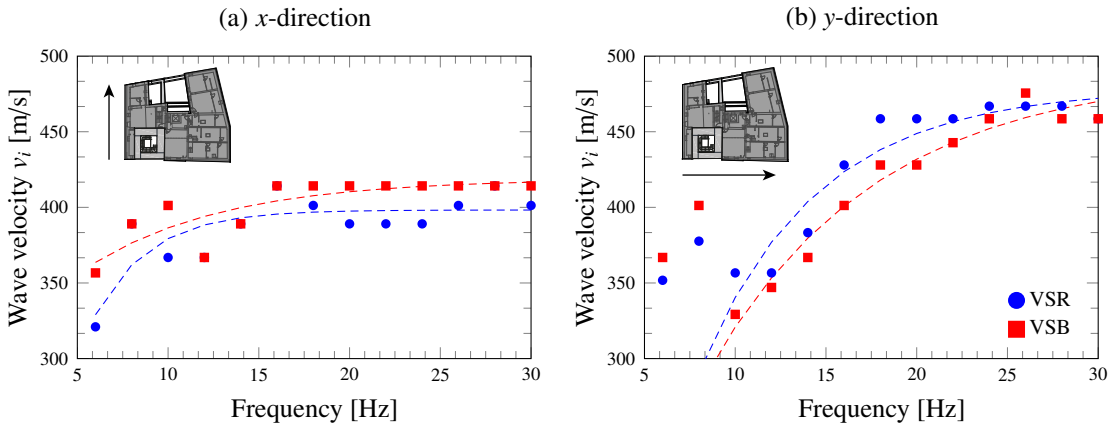

Figure 9. Dispersion curves in the x- (a) and y- (b) directions obtained by peak-picking analysis of the ambient noise low-pass filtered IRFs in the Sciri Tower (F_s = 200 Hz). The dashed lines stand for an exponential regression model $y = a - b\exp(-cx)$, with fitting coefficients a = 398.2510, b = 485.7090, c = 0.3247 for the x−direction and VSR, a = 418.9076, b = 122.8097, c = 0.1330 for the x−direction and VSB, a = 478.4612, b = 643.1162 and c = 0.1539 for the y−direction and VSR, and a = 490.0214, b = 491.9954 and c = 0.1068 for the y−direction and VSB.

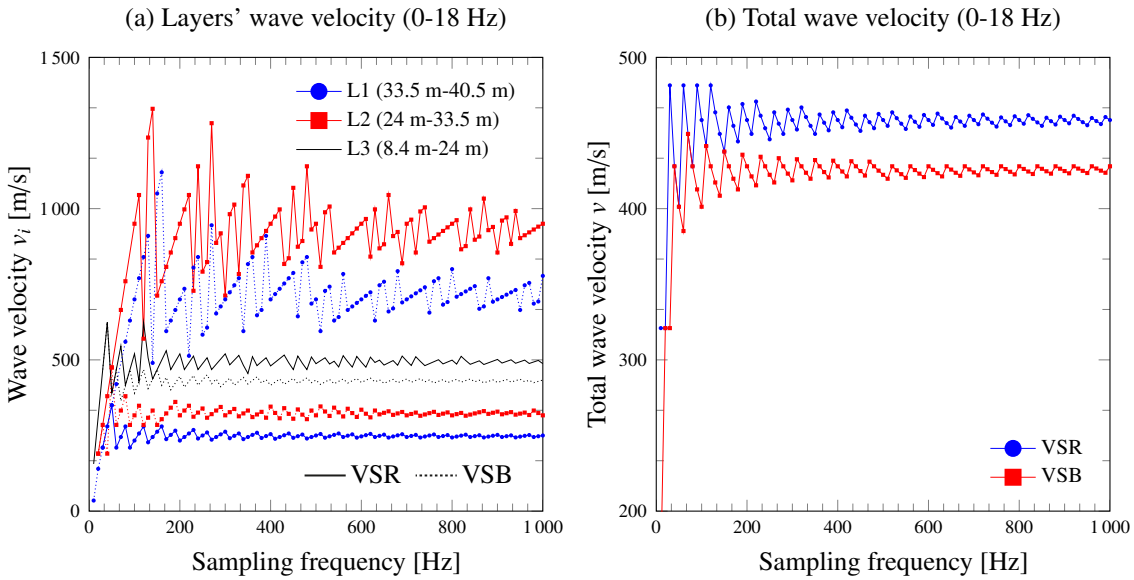

Figure 10. Convergence analysis of the layers' wave velocities (a) and total wave velocity (b) in the y-direction of the Sciri Tower for increasing sampling rates F_s (0-18 Hz).

the attenuation of the waveforms. The amplitude of elastic waves can be attenuated in general due to material and radiation (geometric) damping. Nonetheless, radiation losses in building-type structures usually play a minor role, and the decay of waveforms over time primarily depends on the intrinsic material attenuation converting elastic energy into heat. The material attenuation, also termed quality factor Q, can be computed from the slope S of the natural logarithm of the envelope of the deconvolved waveforms as $Q = \pi f / S$ [25]. Afterwards, the damping ratio ζ can be related to Q as:

$$\zeta = \frac{1}{2Q}. \tag{12}$$

In order to extract the modal damping ratios and mode shapes, the IRFs must be band-pass filtered around the resonant frequencies. In particular, the contributions of modes $F_{x'1}$ and $F_{x'2}$ have been isolated by using frequency bands of 1.6-1.8 Hz and 4.8-5.8 Hz, respectively (see Fig. 11 (a)). On this basis, the resulting waveforms and the natural logarithm of their envelopes are depicted in Figs. 11 (b) and (c), respectively. Since the modal amplitudes of the lowest level are considerably weak (z = 8.4 m), only the top three sensors are used in this analysis. Damping ratios $\zeta_1 = 0.66 \pm 0.08\%$ and $\zeta_2 = 2.4 \pm 0.6\%$ are obtained for the first $F_{x'1}$ and second $F_{x'2}$ bending modes, respectively. Assuming that the damping ratios should be approximately constant along the tower, the error tolerances in ζ_i have been computed as the standard deviation between the ratios obtained at the selected channels. Note that these values are in good agreement with those found by SSI identification (see Table 1). The moderate variability of the estimates can be ascribed to the restraint conditions imposed by the building aggregate, which may yield varying damping ratios along the height of the tower. Finally, the mode shapes can be readily obtained as the amplitude of the band-pass filtered IRFs at $t = 0$ as shown Fig. 11 (b). Note that these mode shapes correspond to the projection of those previously shown in Fig. 6 onto the y-z plane.

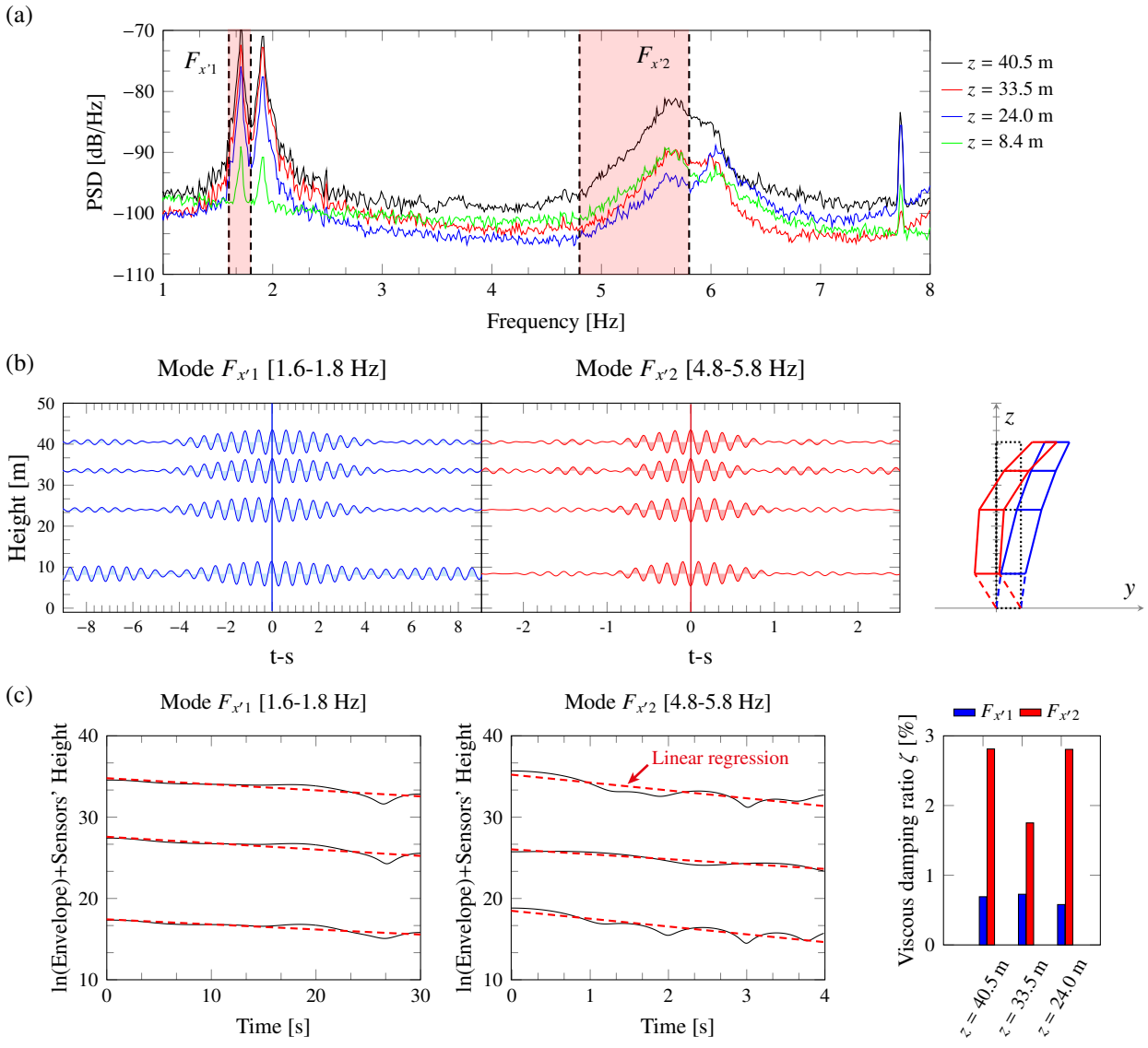

Figure 11. Power Spectral Density (PSD) of the ambient vibration records at different heights of the Sciri Tower in the y-direction (a), band-pass filtered IRFs and mode shapes (b), and natural logarithm of the envelopes of the waveforms (c). In order to extract the separate properties of the natural modes $F_{x'1}$ and $F_{x'2}$, band-pass filters of 1.6-1.8 Hz and 4.8-5.8 Hz are considered (channels 2, 5, 8 and 11, F_s = 200 Hz).

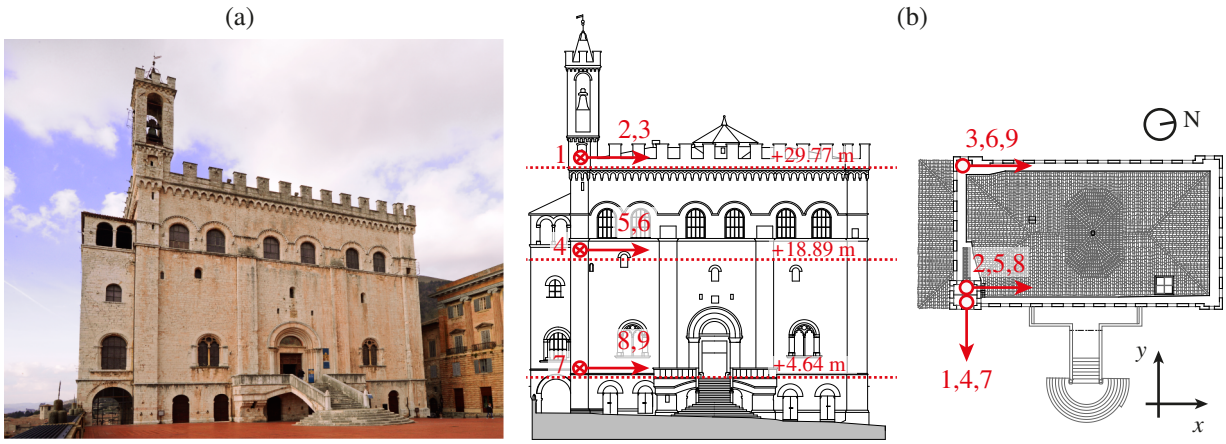

Figure 12. View of the Consoli Palace (a), and sketch of the structural monitoring system (b) with sensors positions (from 1 to 9).

4 Case II: Consoli Palace

The Consoli Palace (*Palazzo dei Consoli*) is the most emblematic monument of the historical city centre of Gubbio in Italy (Fig. 12 (a)). Under design of the architect Angelo da Orvieto and the surveyor Matteo Gattapone, the palace was built between 1332 and 1349 to house all the official courts of the Free Comune of Gubbio. The construction required deep transformations of the natural layout of the site. This included a vaulted hanging solution in the central square named Piazza Grande in order to interconnect the monumental ensemble, which represents today the biggest hanging square in the world. Since 1901, the Consoli Palace has hosted the Civic Museum, and houses a large collection of art masterpieces, including ceramics, archaeological and oriental collections, as well as an extensive section dedicated to the unification of Italy (1848-1860). The collection includes the famous Iguvine Tablets, a series of seven bronze tables from the ancient Umbrian civilization dating back to around the 3rd century before Christ.

The Consoli Palace dominates the urban landscape of Gubbio from its height of 60 m with its bell-tower and panoramic loggia. Built in Gothic style with calcareous stone masonry and an articulated internal distribution of volumes, the building has a rectangular plan of about 40×20 m and is constituted by thick bearing walls and masonry vaults as horizontal elements. Due to the steep slope of the mountain where it was erected, the foundations are placed on two levels with a drop of approximately 10 m beneath the loggia on the south façade. The main façade faces Piazza Grande and is presided over by a fan-shaped staircase entrance and an arched portal. In the upper part, the façade is architecturally characterized by arched-topped windows placed in couples separated by lesenes, as well as a top crown of merlons supported by ogival arches. Since the 19th century, several restoration interventions have been carried out, including the re-building of the entrance staircase, seismic retrofitting operations after the earthquakes of the early 1980s, cleaning operations of façades and interior walls, and restoration of wooden external portals and doors.

In this section, the ambient vibrations recorded by Kita and co-authors[12] in an AVT conducted on May 4th 2017 are used to identify the travelling waves in the building. The AVT was conducted using 11 uni-axial high sensitivity piezoelectric accelerometers, model PCB 393B12, capable of measuring accelerations of ±0.50 g with a sensitivity of 10 V/g. Nonetheless, in this work, only 9 accelerometers monitoring the x- and y-directions along the height of the Palace are used as sketched in Fig. 12 (b). These accelerometers were deployed on the three main floors of the palace at heights of 4.64, 18.89 and 29.77 m, respectively. The sensors were connected to a multi-channel data acquisition system, model NI CompactDAQ-9132, having 24-bit resolution, 102 dB dynamic range and anti-aliasing filters. Ambient vibration data were collected in six separate 30 min long files at a sampling frequency of 1652 Hz. Table 4 summarizes the resonant frequencies and damping ratios of the building obtained by SSI. It is noted that six different modes of vibration were identified in frequencies up to 10 Hz. These include two flexural modes in the x- and y-directions, F_{x1} and F_{y1}, respectively, one torsional mode, $T1$, and, finally, three local modes involving the bell-tower and denoted as $L1$, $L2$ and $L3$. For more information on the results of the OMA identification, readers can refer to reference[12].

Table 4. Experimentally identified natural frequencies of the Consoli Palace from AVT by SSI.

Mode no.	Mode type	f_i^{SSI} [Hz]	ζ^{SSI} [%]
1	F_{x1}	2.296	1.121
2	F_{y1}	2.990	0.751
3	$L1$	3.508	0.779
4	$L2$	3.734	2.477
5	$T1$	4.174	1.104
6	$L3$	7.049	1.089

4.1 Convergence study of multiple-window stacking of ambient-vibration data

In this case study, the duration of the test was 180 minutes, and it is possible to perform the wave deconvolution using time windows as previously reported in Section 2.3. To do so, a convergence analysis of the deconvolved waveforms for increasing time lengths is conducted in Fig. 13 based upon the root-mean-square misfit proposed by Prieto *et al.*[37]:

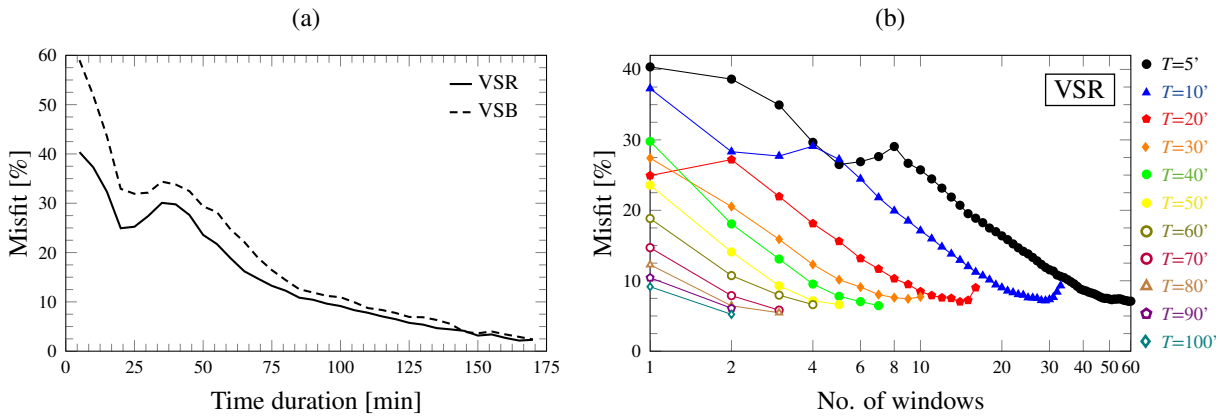

Figure 13. Convergence tests of ambient noise interferometry in the y-direction (channels 1,4,7) of the Consoli Palace in terms of rms misfit, considering a sampling frequency of F_s = 200 Hz and band-pass filtered waveforms with cut-off frequencies of 2-9 Hz. Firstly, the misfits are computed for deconvolved waveforms considering different time durations (a) and, secondly, the misfits are obtained considering stacked time windows with 50% overlap (b). Labels VSR and VSB stand for virtual source at the roof and the base levels, respectively.

$$\text{Misfit}(z,h) = \sqrt{\frac{\int_{t_a}^{t_b} [D_T(z,t) - D_{all}(z,t)]^2 \, \mathrm{d}t}{\int_{t_a}^{t_b} [D_{all}(z,t)]^2 \, \mathrm{d}t}}, \qquad (13)$$

where t_a and t_b define the time interval used to compute the misfit (-1.5 s and 1.5 s in this study), T is the stacking duration, and $D_T(z,t)$ and $D_{all}(z,t)$ are the deconvolved IRFs at height z stacked over the time period T and using the entire data set, respectively. The level of ambient vibration during the test was considerably low, with accelerations not exceeding 0.0015 m/s^2, whereby a thorough pre-processing of the signals has been crucial. Specifically, time domain filtering applying Hanning windows has been performed to eliminate undesired noise sources such as spikes related to electrical interferences, as well as the non-stationary excitation produced by the swinging bells of the bell-tower. Figure 13 (a) shows the convergence of the deconvolved waveforms for increasing time lengths between 5 and 170 minutes. In this figure, the waveforms are band-pass filtered with cut-off frequencies of 2-9 Hz in order to isolate the contribution of the first six vibration modes. In general, it is observed that the computed misfits decrease quickly with the time duration, reaching a value of 10% at around 137 minutes. Nevertheless, a stable convergence is not reached during the AVT, which may indicate the influence of environmental (e.g. temperature variations) or operational effects. Then, a second convergence analysis is presented in Fig. 13 (b) considering time windows of different duration, and stacked along the complete duration of the test. In particular, time windows ranging between 5 and 100 min are considered with 50% overlap. It is noted in this figure that longer time windows lead to faster convergence rates. Moreover, it is observed in all the cases that the misfit decreases for an increasing number of stacked windows. Time windows of 10 minutes with 50% overlap reach a misfit of 10% for around 35 windows, which is assumed accurate enough for the aim of the subsequent analyses.

4.2 Convergence study on the data acquisition sampling rate

The convergence of the identified wave arrival times t_i with increasing frequency sampling rates F_s is presented in Fig. 14. In this case, a wider frequency band of 2-16 Hz is considered to facilitate the identification of travelling pulses at the mid-height of the palace. It is observed in this figure that convergence is quickly achieved for sampling frequencies above 100 Hz, thereby F_s=100 Hz is selected in the subsequent analyses. Furthermore, it is observed that the global time of the waves to cross the whole building considering virtual sources at the base and roof levels are very similar (z = 4.64 m and 29.77 m for VSR and VSB schemes, respectively), while some discrepancies are found at the central height z = 18.89 m. This fact indicates some limitations in the accuracy of the estimates of local wave velocities in the building due to the reduced separation between the sensors.

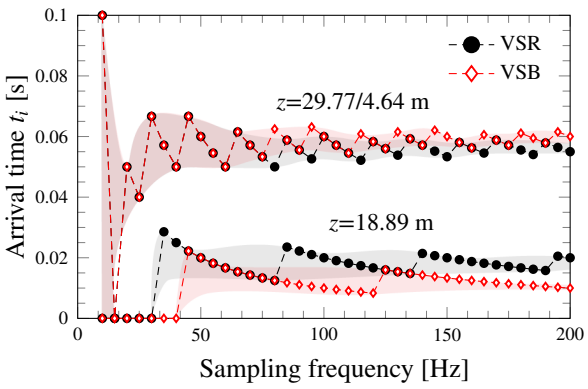

Figure 14. Convergence analysis of wave arrival times t_i for increasing frequency sampling rates F_s (2-16 Hz, y-direction, channels 1,4,7). Virtual sources at the roof and the base levels are labelled with VSR and VSB, respectively.

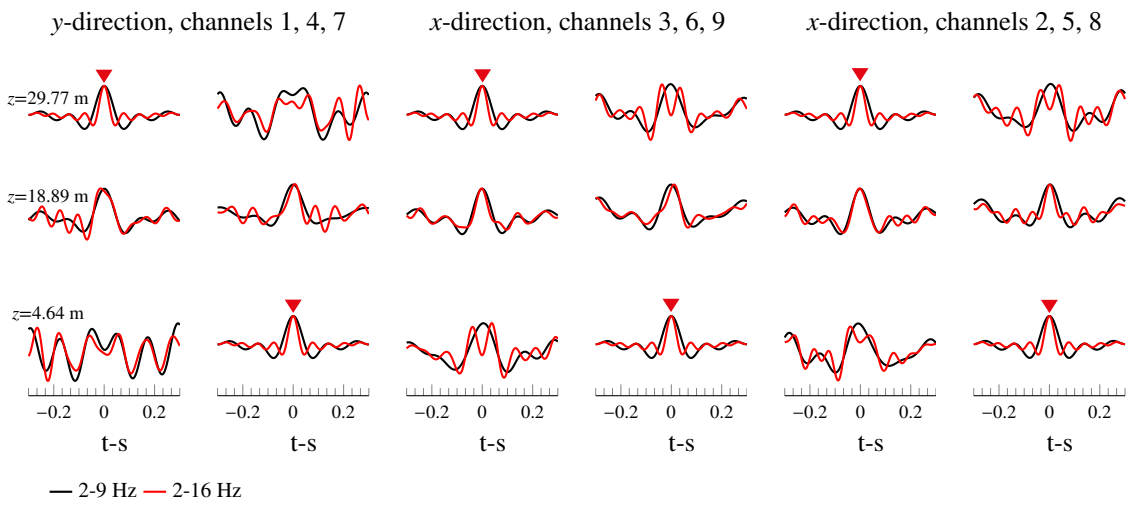

Figure 15. Band-pass filtered IRFs in the Consoli Palace considering different frequency bands, namely 2-9 Hz and 2-16 Hz, and stacked considering time windows of 10 minutes with 50% overlap (F_s=100 Hz).

4.3 Stacked band-pass filtered waveforms

Figure 15 shows the stacked waveforms in the y-direction (channels 1, 4, and 7) and the x-direction (channels 3, 6, and 9, and channels 2, 5, and 8) using time windows of 10 min with 50% overlap and sampling frequency F_s=100 Hz. In addition, two different frequency bands are considered, namely 2-9 Hz and 2-16 Hz. It is noted in this figure that travelling pulses in the frequency band 2-9 Hz can be only identified in the y-direction. Conversely, travelling pulses can be identified in both directions when the wider frequency band 2-16 Hz is considered. This is due to the limited separation between the sensors and, according to the previous discussion in Section 2.2, a wider frequency band is required to minimize the width of the pulses. It can be visually noted that waves travel faster in the x-direction and, as a result, travelling pulses can be only identified in the second frequency band. It is also interesting to observe in the y-direction that waves travel slower in the second frequency band and, therefore, the dispersion relation exhibits a different behaviour to that in the previous case study. This fact suggests that the geometrical complexity of the structure may favour the appearance of multiple reflections along its height, resulting in a complicated dispersion relation. Finally, Table 5 reports the global wave delays τ and velocities v obtained by peak-picking analysis in the y- and x-directions of the Consoli Palace. Note that, owing to the larger stiffness of the building in the x-direction, the velocity of the waves is higher in this direction. Moreover, good agreements are found between the estimates considering virtual sources either at the roof level (VSR, z = 29.77 m) or the base level (VSB, z = 4.64 m), what demonstrates the accuracy of the wave identification.

5 Case III: Bell-tower of the Basilica of San Pietro

This last illustrative case study is the bell-tower of the Basilica of San Pietro located in the southern part of the city of Perugia, Italy (see Fig. 16 (c)). The construction of the monastery dates back to around 996, although the bell-tower was not erected until the 13th century. The Benedictine abbey is an architectural ensemble arranged around three main cloisters, comprising the basilica, a convent and other more recent buildings. Over the centuries, the bell-tower has been subjected to several architectural alterations and restoration interventions. The current configuration dates back to the 15th century, and the design is attributed to the architect Bernardo Rossellino. Three main structural portions can be identified in the tower, including the shaft, the belfry and the cusp. Firstly, the shaft stands 26 m high and has a dodecagonal cross-section. The bulk of the shaft is made of stone masonry with large external portions of brick masonry as a result of several rehabilitation operations. Rising up to a height of 40.8 m, an hexagonal belfry sits on top of the shaft. The belfry is made of brick masonry covered with an external curtain of stone, and large Gothic mullioned windows characterize its architecture. Finally, a brick masonry cusp completes the tower with a total height of 61.4 m. The bell-tower stands out between the basilica and other branches of the abbey, being its first 17 m restrained by the adjoining buildings. In 1997, the tower was severely damaged after the Umbria–Marche earthquake, so it was painstakingly restored and consolidated in 2001.

As reported by Ubertini *et al.*[14], the 2016 Central Italy seismic sequence produced moderate damage in the bell-tower with permanent variations in its modal properties. The seismic sequence consisted of the Accumoli M_w 6.0 earthquake of August 24th, followed by the Ussita M_w 5.9 and Norcia M_w 6.5 earthquakes of October 26th and 30th, respectively. Albeit only small peak ground accelerations of 30 cm/s^2 were measured in the vicinity of the tower (85 km far from the epicentre of the first major shock), the OMA of acceleration records demonstrated cumulated permanent decays in the natural frequencies of the tower[14]. While no significant damages could be visually identified, the non-linear finite element simulations by Cavalagli *et al.*[43] corroborated the experimental results and reported the development of microcracks at the base of the columns of the belfry. In this light, this case study constitutes a remarkable example of the effectiveness of SHM for early-stage earthquake-induced damage detection.

Table 5. Identified global wave delays τ and velocities v in the Consoli Palace (windows of 10 min with 50% overlap, F_s = 100 Hz).

	y-direction, channels 1, 4, 7				*x*-direction, channels 3, 6, 9				*x*-direction, channels 2, 5, 8			
	2-9 Hz		2-16 Hz		2-9 Hz		2-16 Hz		2-9 Hz		2-16 Hz	
	VSR	VSB	VSR	VSB	VSR	VSB	VSR	VSB	VSR	VSB	VSR	VSB
τ [ms]	50	40	60	60	-	-	40	40	-	-	40	40
v [m/s]	502.60	628.25	418.83	418.83	-	-	628.25	628.25	-	-	628.25	628.25

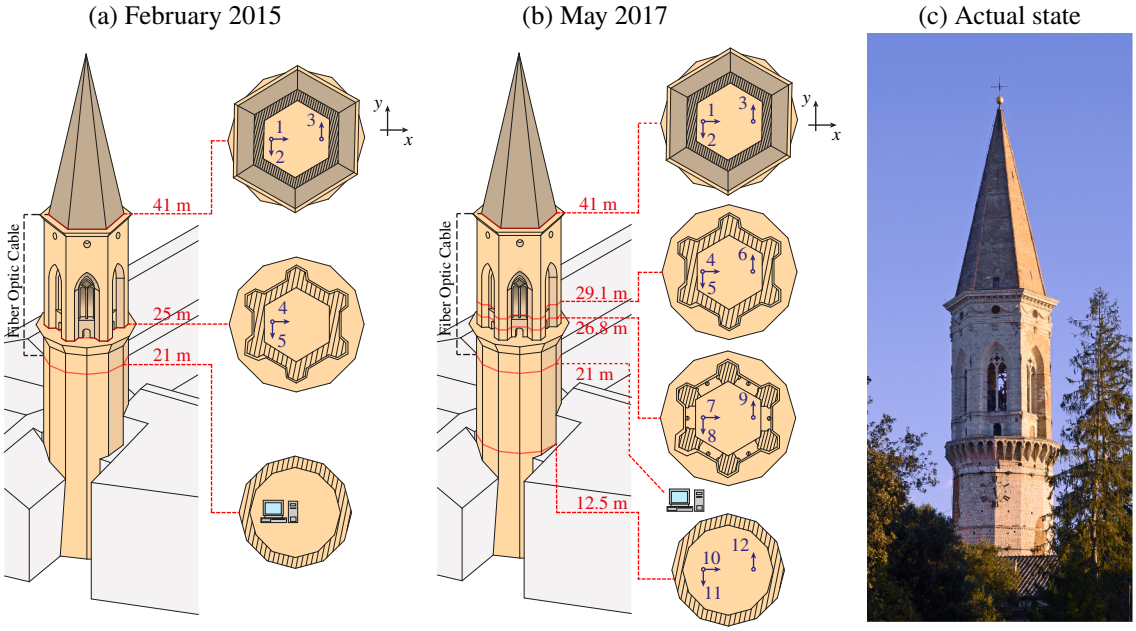

Figure 16. Sketch of the AVT conducted in February 2015 (a), May 2017 (b), and view of the masonry bell-tower of the Basilica of San Pietro (c).

In this work, two AVTs, carried out before and after the 2016 Central Italy seismic sequence, are used to assess the earthquake-induced damage effects through OMA and ambient noise seismic interferometry. The first AVT was carried out in February 2015 by using five high-sensitivity (10 V/g) accelerometers, model PCB 393B12. As sketched in Fig. 16 (a), the sensors were placed at two different levels, namely z = 41 m and z = 25 m, and the acceleration records were collected through a DAQ system located at z = 21 m. On the other hand, the second AVT was carried out in May 2017 and consisted of twelve accelerometers model PCB 393B12 deployed at four different levels as sketched in Fig. 16 (b), namely z = 41 m, z = 29.1 m, z = 26.8 m and z = 12.5 m, as well as a DAQ system located at z = 21 m. In both cases, the ambient vibrations were recorded for 30 minutes at a sampling frequency of 100 Hz.

5.1 Damage detection through operational modal analysis

This section presents the attempts made to detect earthquake-induced damage through OMA of the acceleration series recorded in the AVTs of February 2015 and May 2017. Table 6 presents the comparison between the modal features extracted by means of SSI before and after the seismic sequence. A total of seven modes have been identified in the AVT of May 2017 with resonant frequencies up to 10 Hz, and the mode shapes are depicted in Fig. 17. These include first (Fx1, Fy1), second (Fx2, Fy2), and third flexural modes (Fx3, Fy3), with x and y denoting the prevailing modal direction, as well as a torsional mode T1. The same vibration modes have been found in the AVT of February 2015, except for the mode Fx3, what can be ascribed to limitations in the monitoring of the x-direction of the tower only by channels 1 and 4 (see Fig. 16). The comparison between the modal features has been conducted in terms of *MAC* values (Modal Assurance Criterion), and relative differences between resonant frequencies f_i^{SSI} and damping ratios ζ_i^{SSI}. It is noted that, since the relative differences in terms of resonant frequencies do not show a clear pattern, damage cannot be directly inferred from frequency shifts. Specifically, the natural frequencies of modes Fx1, Fy1 and Fy2 experience increases, while those of modes T1, Fx2 and Fy3 decrease. This is due to the dependence of the resonant frequencies upon environmental effects as reported by Ubertini and co-authors[14]. In particular, those authors reported a strong dependence of resonant frequencies on environmental temperature, whereby damage-induced frequency shifts are masked by daily temperature fluctuations. It is thus imperative to detrend the natural frequencies considering environmental effects in order to identify damage-induced permanent variations through a novelty analysis. This however demands a long-term monitoring and cannot be done with single AVTs and OMA[44]. With regard to the comparison between damping ratios, large reductions for all the vibration modes are reported in Table 6. Nevertheless, it has been extensively reported in the literature that the assessment of damping under ambient vibrations is highly conditioned by the level of

Table 6. Comparison of the experimentally identified modal features of the masonry bell-tower of the Basilica of San Pietro by SSI from AVTs conducted in February 2015 and May 2017.

		February 2015		May 2017				
Mode no.	Mode type	f_i^{SSI} [Hz]	ζ_i^{SSI} [%]	f_i^{SSI} [Hz]	ζ_i^{SSI} [%]	MAC	$100\,\frac{\Delta f_i^{SSI}}{f_i^{SSI}\vert_{2015}}$	$100\,\frac{\Delta \zeta_i^{SSI}}{\zeta_i^{SSI}\vert_{2015}}$
1	Fx1	1.450	1.435	1.461	0.977	0.991	0.759	-31.916
2	Fy1	1.519	1.374	1.533	0.932	0.997	0.922	-32.169
3	T1	4.346	1.893	4.196	1.049	0.985	-3.451	-44.585
4	Fx2	4.569	1.777	4.480	0.915	0.750	-1.948	-48.509
5	Fy2	4.888	2.616	5.001	1.798	0.723	2.312	-31.269
6	Fx3	-	-	7.121	2.092	-	-	-
7	Fy3	7.236	3.074	7.217	2.512	0.789	-0.263	-18.282

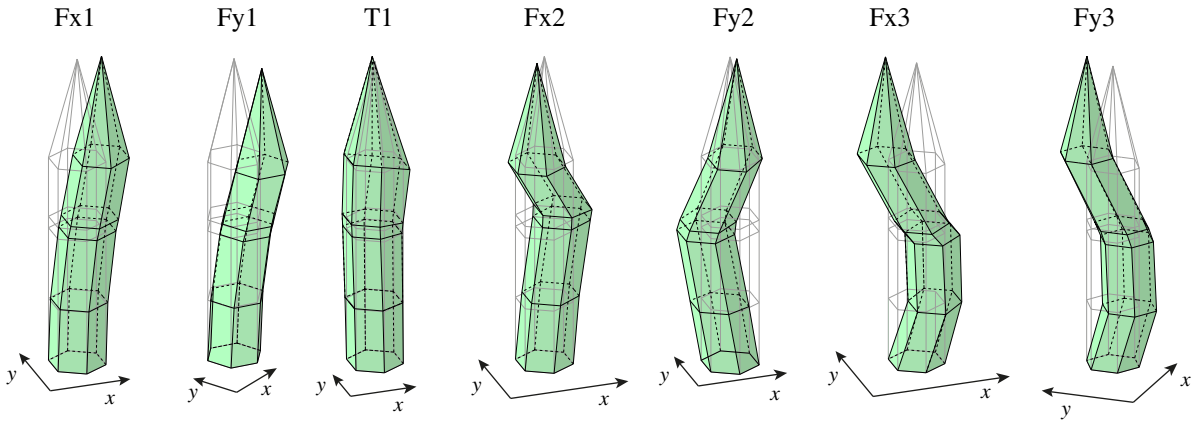

Figure 17. Experimentally identified mode shapes of the Basilica of San Pietro by SSI from the AVT of May 2017.

excitation, which is typically very low in masonry structures. Thus, although some encouraging results can be found on the literature on the use of damping variations as a damage sensitive feature (see e.g.[45]), their use in masonry structures is subjected to a high level of uncertainty. Finally, since mode shapes are presumably less sensitive to temperature, the comparison of *MAC* values can give more insight into the presence of damage. It is noted in Table 6 that the *MAC* values for the modes Fx1, Fy1 and T1 are close to one, that is to say, no significant differences are found before and after the seismic sequence. These modes represent the global stiffness of the structure and, therefore, they are expected to be low sensitive to local damage. Conversely, lower *MAC* values are found for higher order modes in which local stiffness effects play a more relevant role. Therefore, it is concluded that these results may evidence the presence of damage, although its localization would require the inverse calibration of a numerical model.

5.2 Damage detection and localization through ambient noise deconvolution interferometry

Finally, this section investigates the potential application of deconvolution interferometry as a complementary approach to OMA for damage detection and localization. Figure 18 shows the low-pass filtered IRFs in the x-direction of the masonry bell-tower considering different frequency bands, namely 0-11 Hz, 0-15 Hz and 0-20 Hz, obtained from the AVTs conducted in February 2015 (a) and May 2017 (b). Similar results are obtained in the y-direction and, therefore, specific analyses in this direction are omitted because of space constraints. In both AVTs, two clear causal and acausal pulses can be identified, whereby the wave velocities can be readily obtained by peak-picking the wave arrival times. Figure 19 shows the computed wave velocities as functions of the cut-off frequency. Taking advantage of the larger sensor density in the AVT of May 2017, the wave velocities are obtained in this case between the heights 12-41 m (global velocity accounting for both the shaft and belfry areas, channels 1 and 10) and 26.8-41 m (local velocity isolating the belfry area, channels 1 and 7), denoted with asterisk and double asterisk in Fig. 19, respectively. It can be clearly observed that the 2016 Central Italy seismic sequence produced reductions in the wave velocities, that is to say, stiffness losses due to earthquake-induced damages. In particular, relative reductions of 4.97%, 10.11% and 9.36% are obtained in terms of global velocity for cut-off frequencies of 11 Hz, 15 Hz and 20 Hz, respectively. On the other hand, larger reductions of 19.90%, 16.34% and 21.69% are obtained in terms of local velocity in the area of the belfry for cut-off frequencies of 11 Hz, 15 Hz and 20 Hz, respectively. These variations are consistent with the experimental results presented by Ubertini and co-authors[14], who reported cumulated decays in the temperature-detrended resonant frequencies of 7.58%, 5.74%, 10.81%, 5.08% and 3.98% for the modes F_{x1}, F_{y1}, T_1, F_{y2} and F_{y3}, respectively. In addition, in view of the larger reductions in wave velocity observed in the belfry, these results also confirm the localization of damage in this area showed by the numerical simulations of Cavalagli *et al.*[43]. Therefore, these results demonstrate the applicability of ambient noise interferometry for damage

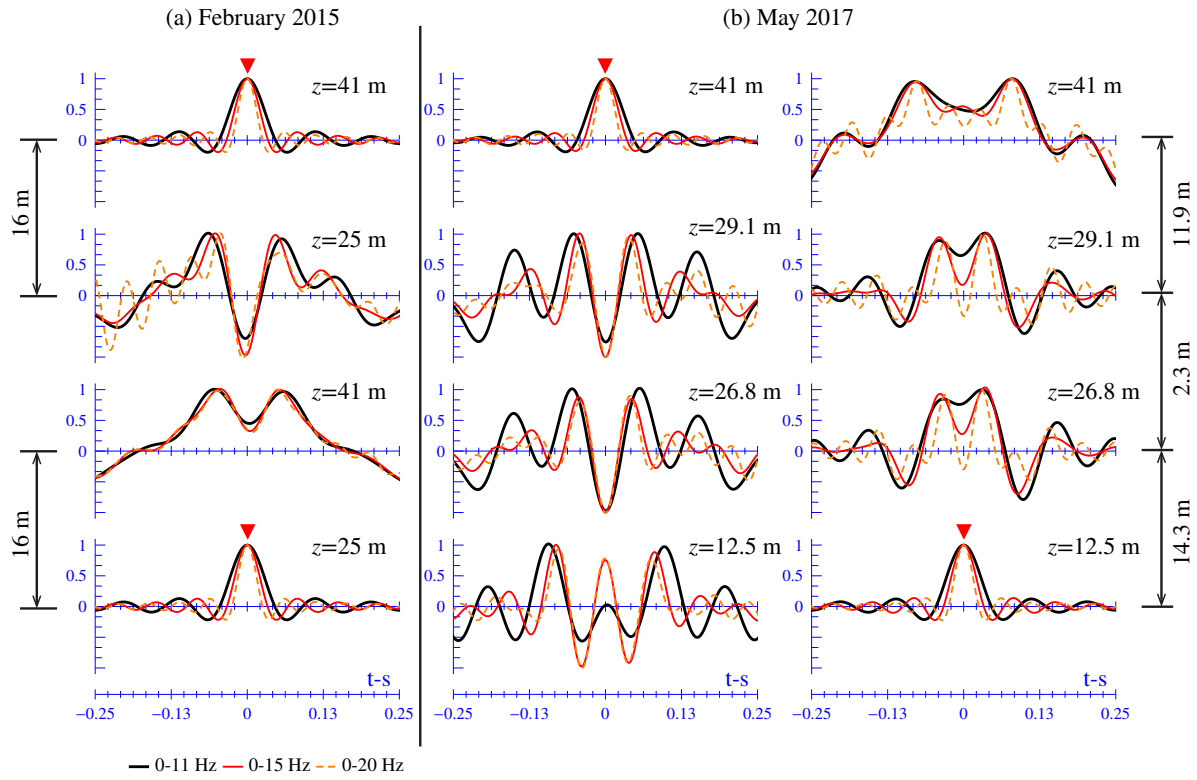

Figure 18. Low-pass filtered IRFs in the x-direction of the masonry bell-tower of the Basilica of San Pietro considering different frequency bands, namely 0-11 Hz, 0-15 Hz and 0-20 Hz, obtained from the AVTs conducted in February 2015 (channels 1 and 4) (a) and May 2017 (channels 1, 4, 7 and 10) (b) (30 minutes AVT, F_s=100 Hz).

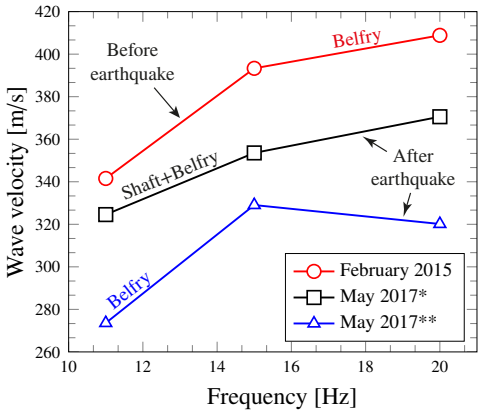

Figure 19. Wave velocities versus cut-off frequency obtained by peak-picking analysis of low-pass filtered IRFs computed on the basis of the AVTs conducted in February 2015 (before earthquake) and May 2017 (after earthquake) in the masonry bell-tower of the Basilica of San Pietro (30 minutes, F_s=100 Hz). Asterisk and double asterisk denote computed velocities in the height ranges 41-12.5 m (shaft and belfry areas) and 41-26.8 m (isolated belfry area), respectively.

detection, localization and, to some extent, quantification in masonry structures. In addition, it may be concluded that the velocity of shear waves in masonry structures is less sensitive to temperature than natural frequencies. Since the resonant frequencies and shear wave velocities in beam-like structures are proportional to $\sqrt{E}$ and $\sqrt{G}$[34], respectively, with E and G being Young's modulus and shear modulus, the closure of micro-cracks due to temperature-induced material expansion may manifest through larger equivalent Young's moduli with smaller variations of shear modulus. Nonetheless, these results must be taken with caution due to potential sampling limitations. Specifically, the minimum observable variation in the global wave velocity obtained by Eq. (10) and a sampling frequency of F_s = 100 Hz is 49.82 m/s, which supposes 15% of the global velocity obtained in the AVT of February 2015 with a cut-off frequency of 11 Hz. Therefore, in-depth analyses with larger data acquisition sampling rates and long-term monitoring should be pursued in future research works to delve into the possible daily changes induced by temperature fluctuations.

6 Conclusions

This paper has presented the synergistic application of OMA and ambient noise deconvolution interferometry for structural and damage identification in three Italian historic masonry structures, including the Sciri Tower in Perugia, the Consoli Palace in Gubbio, and the bell-tower of the Basilica of San Pietro in Perugia. Firstly, wave propagation analyses have been conducted on the basis of an AVT carried out in the Sciri Tower in order to investigate different aspects covering the identification of wave velocities, namely the effects of low-pass and band-pass filters, degree of dispersion, and convergence analyses for increasing frequency sampling rates, as well as the identification of mode shapes and viscous damping ratios. Afterwards, the Consoli Palace has been presented as a case study of a complex masonry building with limited distance between the sensors. In this case, the study has focused on the robustness of the identification of wave velocities through peak-picking analysis for increasing monitoring time and sampling rates. Finally, the bell-tower

of the Basilica of San Pietro has been presented as a case study of damage identification. To do so, two different AVTs conducted in February 2015 and May 2017, that is before and after the 2016 Central Italy seismic sequence, have been used. The results have demonstrated that OMA is primarily effective for detecting the presence of damage, and that the use of deconvolution interferometry offers superior capabilities for damage identification, including localization and quantification. Consistently with previously reported decays in the temperature-detrended resonant frequencies of the tower, the reported results have shown reductions in the wave velocities between 5% and 10% in the areas of the shaft and belfry of the tower, while larger reductions between 16% and 22% have been found in the isolated area of the belfry for frequencies between 11 Hz and 20 Hz.

Overall, this paper has illustrated, for the first time in the literature, the potentials of ambient noise interferometry for structural identification and early-stage damage identification in historic masonry structures. Most of the technical aspects regarding the monitoring and processing of the measurements have been covered, whereby this work is envisaged to pave the way for future long-term continuous monitoring applications based on deconvolution interferometry.

Acknowledgement

This work was supported by the Italian Ministry of Education, University and Research (MIUR) through the funded project of national interest "SMART-BRICK: novel strain-sensing nanocomposite clay brick enabling self-monitoring masonry structures" (Protocol No. 2015M55L27).

References

1. E. P. Carden, P. Fanning, Vibration based condition monitoring: a review, Structural Health Monitoring 3 (2004) 355–377.
2. M. G. Masciotta, L. F. Ramos, P. B. Lourenço, The importance of structural monitoring as a diagnosis and control tool in the restoration process of heritage structures: a case study in Portugal, Journal of Cultural Heritage 27 (2017) 36–47.
3. X. Kong, J. Li, W. Collins, C. Bennett, S. Laflamme, H. Jo, Sensing distortion-induced fatigue cracks in steel bridges with capacitive skin sensor arrays, Smart Materials and Structures 27 (2018) 115008.
4. W. Fan, P. Qiao, Vibration-based damage identification methods: a review and comparative study, Structural Health Monitoring 10 (2011) 83–111.
5. E. Reynders, System identification methods for (operational) modal analysis: review and comparison, Archives of Computational Methods in Engineering 19 (2012) 51–124.
6. B. J. A. Costa, F. Magalhães, Á. Cunha, J. Figueiras, Rehabilitation assessment of a centenary steel bridge based on modal analysis, Engineering Structures 56 (2013) 260–272.
7. P. Pachón, R. Castro, E. García-Macías, V. Compan, E. Puertas, E. Torroja's bridge: Tailored experimental setup for SHM of a historical bridge with a reduced number of sensors, Engineering Structures 162 (2018) 11–21.
8. C. Gentile, M. Guidobaldi, A. Saisi, One-year dynamic monitoring of a historic tower: damage detection under changing environment, Meccanica 51 (2016) 2873–2889.
9. S. Ivorra, D. Foti, V. Gallo, V. Vacca, D. Bru, Bell's dynamic interaction on a reinforced concrete bell tower, Engineering Structures 183 (2019) 965–975.
10. C. Gentile, C. Poggi, A. Ruccolo, M. Vasic, Vibration-Based Assessment of the Tensile Force in the Tie-Rods of the Milan Cathedral, International Journal of Architectural Heritage (2019) 1–14.
11. L. F. Ramos, R. Aguilar, P. B. Lourenço, Operational modal analysis of historical constructions using commercial wireless platforms, Structural Health Monitoring 10 (2011) 511–521.
12. A. Kita, N. Cavalagli, F. Ubertini, Temperature effects on static and dynamic behavior of Consoli Palace in Gubbio, Italy, Mechanical Systems and Signal Processing 120 (2019) 180–202.
13. W. Soo Lon Wah, Y. T. Chen, G. W. Roberts, A. Elamin, Separating damage from environmental effects affecting civil structures for near real-time damage detection, Structural Health Monitoring 17 (2018) 850–868.
14. F. Ubertini, N. Cavalagli, A. Kita, G. Comanducci, Assessment of a monumental masonry bell-tower after 2016 Central Italy seismic sequence by long-term SHM, Bulletin of Earthquake Engineering 16 (2018) 775–801.
15. J. F. Claerbout, Synthesis of a layered medium from its acoustic transmission response, Geophysics 33 (1968) 264–269.
16. E. Şafak, Wave-propagation formulation of seismic response of multistory buildings, Journal of Structural Engineering 125 (1999) 426–437.
17. M. I. Todorovska, S. S. Ivanović, M. D. Trifunac, Wave propagation in a seven-story reinforced concrete building: I. Theoretical models, Soil Dynamics and Earthquake Engineering 21 (2001) 211–223.
18. K. Wapenaar, D. Draganov, R. Snieder, X. Campman, A. Verdel, Tutorial on seismic interferometry: Part 1–Basic principles and applications, Geophysics 75 (2010) 75A195–75A209.
19. R. Snieder, M. Miyazawa, E. Slob, I. Vasconcelos, K. Wapenaar, A comparison of strategies for seismic interferometry, Surveys in Geophysics 30 (2009) 503–523.
20. M. I. Todorovska, M. D. Trifunac, Earthquake damage detection in the Imperial County Services Building III: analysis of wave travel times via impulse response functions, Soil Dynamics and Earthquake Engineering 28 (2008) 387–404.
21. M. I. Todorovska, M. D. Trifunac, Impulse response analysis of the Van Nuys 7-storey hotel during 11 earthquakes and earthquake damage detection, Structural Control and Health Monitoring: The Official Journal of the International Association for Structural Control and Monitoring and of the European Association for the Control of Structures 15 (2008) 90–116.
22. M. Rahmani, M. Ebrahimian, M. I. Todorovska, Time-wave velocity analysis for early earthquake damage detection in buildings: Application to a damaged full-scale RC building, Earthquake Engineering & Structural Dynamics 44 (2015) 619–636.
23. D. S. Singh, S. Gupta, A. Ray, Online recursive estimation of remaining life using ultrasonic measurements, Structural Health Monitoring 11 (2012) 413–421.
24. M. I. Todorovska, M. T. Rahmani, System identification of buildings by wave travel time analysis and layered shear beam models–Spatial resolution and accuracy, Structural Control and Health Monitoring 20 (2013) 686–702.

25. R. Snieder, E. Şafak, Extracting the building response using seismic interferometry: Theory and application to the Millikan Library in Pasadena, California, Bulletin of the Seismological Society of America 96 (2006) 586–598.
26. M. I. Todorovska, Seismic interferometry of a soil-structure interaction model with coupled horizontal and rocking response, Bulletin of the Seismological Society of America 99 (2009) 611–625.
27. M. I. Todorovska, Soil-structure system identification of Millikan Library North-South response during four earthquakes (1970-2002): What caused the observed wandering of the system frequencies?, Bulletin of the Seismological Society of America 99 (2009) 626–635.
28. C. Michel, P. Guéguen, S. El Arem, J. Mazars, P. Kotronis, Full-scale dynamic response of an RC building under weak seismic motions using earthquake recordings, ambient vibrations and modelling, Earthquake Engineering & Structural Dynamics 39 (2010) 419–441.
29. S. S. Ivanovic, M. D. Trifunac, M. D. Todorovska, On identification of damage in structures via wave travel times, in: Strong Motion Instrumentation for Civil Engineering Structures, Springer, 2001, pp. 447–467.
30. A. Cabboi, C. Gentile, A. Saisi, From continuous vibration monitoring to FEM-based damage assessment: application on a stone-masonry tower, Construction and Building Materials 156 (2017) 252–265.
31. R. Ghiasi, M. R. Ghasemi, M. Noori, Comparative studies of metamodeling and AI-Based techniques in damage detection of structures, Advances in Engineering Software 125 (2018) 101–112.
32. M. D. Trifunac, S. S. Ivanović, M. I. Todorovska, Wave propagation in a seven-story reinforced concrete building: III. Damage detection via changes in wavenumbers, Soil Dynamics and Earthquake Engineering 23 (2003) 65–75.
33. M. D. Kohler, T. H. Heaton, S. C. Bradford, Propagating waves in the steel, moment-frame factor building recorded during earthquakes, Bulletin of the Seismological Society of America 97 (2007) 1334–1345.
34. M. Ebrahimian, M. I. Todorovska, Wave propagation in a Timoshenko beam building model, Journal of Engineering Mechanics 140 (2013) 04014018.
35. M. Ebrahimian, M. I. Todorovska, Structural system identification of buildings by a wave method based on a nonuniform Timoshenko beam model, Journal of Engineering Mechanics 141 (2015) 04015022.
36. M. Ebrahimian, M. Rahmani, M. I. Todorovska, Nonparametric estimation of wave dispersion in high-rise buildings by seismic interferometry, Earthquake Engineering & Structural Dynamics 43 (2014) 2361–2375.
37. G. A. Prieto, J. F. Lawrence, A. I. Chung, M. D. Kohler, Impulse response of civil structures from ambient noise analysis, Bulletin of the Seismological Society of America 100 (2010) 2322–2328.
38. N. Nakata, R. Snieder, Monitoring a building using deconvolution interferometry. II: Ambient-vibration analysis, Bulletin of the Seismological Society of America 104 (2013) 204–213.
39. D. Bindi, B. Petrovic, S. Karapetrou, M. Manakou, T. Boxberger, D. Raptakis, K. D. Pitilakis, S. Parolai, Seismic response of an 8-story RC-building from ambient vibration analysis, Bulletin of Earthquake Engineering 13 (2015) 2095–2120.
40. H. Sun, A. Mordret, G. A. Prieto, M. N. Toksöz, O. Büyüköztürk, Bayesian characterization of buildings using seismic interferometry on ambient vibrations, Mechanical Systems and Signal Processing 85 (2017) 468–486.
41. G. Lacanna, M. Ripepe, M. Coli, R. Genco, E. Marchetti, Full structural dynamic response from ambient vibration of Giotto's bell tower in Firenze (Italy), using modal analysis and seismic interferometry, NDT & E International 102 (2019) 9–15.
42. A. Kita, N. Cavalagli, G. Comanducci, F. Ubertini, Dynamic testing and monitoring of historic towers for seismic damage detection, in: M. Papadrakakis, M. Fragiadakis (Eds.), 6th ECCOMAS Thematic Conference on Computational Methods in Structural Dynamics and Earthquake Engineering, pp. 2564–2577.
43. N. Cavalagli, G. Comanducci, F. Ubertini, Earthquake-induced damage detection in a monumental masonry bell-tower using long-term dynamic monitoring data, Journal of Earthquake Engineering 22 (2018) 96–119.
44. F. Ubertini, G. Comanducci, N. Cavalagli, Vibration-based structural health monitoring of a historic bell-tower using output-only measurements and multivariate statistical analysis, Structural Health Monitoring 15 (2016) 438–457.
45. M. S. Cao, G. G. Sha, Y. F. Gao, W. Ostachowicz, Structural damage identification using damping: a compendium of uses and features, Smart Materials and Structures 26 (2017) 043001.